Internal Report
LAL/RT 00-07
June 2000

Laboratoire de l'Accélérateur Linéaire

Contributions to the 1999 Particle Accelerator Conference

March 29 - April 2, 1999, New York City, USA

Laboratoire de l'Accélérateur Linéaire
IN2P3-CNRS et Université de Paris-Sud, BP 34, F-91898 Orsay Cedex

U.E.R
de
l'Université Paris-Sud

Institut National
de Physique Nucléaire
et de Physique des Particules

B.P. 34 ~ Bâtiment 200 ~ 91898 ORSAY CEDEX

Internal Report
LAL/RT 00-07
June 2000

Contributions to the 1999 Particle Accelerator Conference

March 29 - April 2, 1999, New York City, USA

Laboratoire de l'Accélérateur Linéaire
IN2P3-CNRS et Université de Paris-Sud, BP 34, F-91898 Orsay Cedex

PLEASE BE AWARE THAT
ALL OF THE MISSING PAGES IN THIS DOCUMENT
WERE ORIGINALLY BLANK

Table of contents

Proceedings of the 1999 Particle Accelerator Conference, New York, 1999

EVIDENCE FOR A STRONGLY COUPLED DIPOLE MODE WITH INSUFFICIENT DAMPING IN TTF FIRST ACCELERATING MODULE

S. Fartoukh, M. Jablonka, J. M. Joly, M. Lalot, C. Magne, O. Napoly, CEA/Saclay, France
M. Bernard, LAL/Orsay, France,
N. Baboi, S. Schreiber, S. Simrock, H. Weise, DESY/Hamburg, Germany

Abstract

A beam experiment has been conducted on the first accelerating module of the TESLA Test Facility (TTF) to investigate transverse higher order modes (HOM) in the superconducting cavities. By injecting the beam with a transverse offset and by modulating the intensity of the 216 MHz bunch train with a tunable frequency in the 0-108 MHz range, transverse HOMs can be excited resonantly. On a resonance the outgoing bunch orbits, measured with a broadband BPM, are transversely modulated at the same frequency. A dipole mode at about 2585 MHz, belonging to the third passband of the TESLA cavities, has been excited and observed in this way, with unexpected low damping in 2 out of the 8 cavities of the module.

1 AIM OF THE EXPERIMENT

The transport of very low emittance beams along the TESLA linac requires transverse higher order mode damping at a level defined in [1]. HOM couplers mounted on the beam tubes of the TESLA 9-cell superconducting cavities, have been designed to achieve damping with Q factors of the order of 10^4 to 10^5, depending on the mode coupling impedance, especially for the first two dipole passbands. Modes from higher passbands, supposedly above cutoff, are expected to propagate and therefore to couple efficiently to the HOM couplers except for few so-called "trapped" modes whose energy is concentrated in the central cells of the cavity. Of the experiments proposed at the TTF to verify with beam that the HOM damping is adequate and to detect unwanted trapped modes, the one reported here, described in [2], consists of excitation of higher order modes with the sidebands of the bunch train $f_b = 216$ MHz harmonics generated by modulation of the bunch charge with a variable frequency F in the range of 0 to 108 MHz. If the beam is injected off axis in the accelerating module, these sidebands build up in the Fourier transform of beam dipole moment and a resonant transverse instability can develop when one of the sidebands and one transverse HOM frequency coincide, i.e. $nf_b \pm F = f_{HOM}$. Hence, at the cavity exit, the transverse position of the beam is modulated at the frequency F with in phase and out of phase components. A broadband BPM can be used to detect these oscillations.

2 EXPERIMENTAL SETUP

The first accelerating module of TTF includes eight 9-cell superconducting cavities at 1.3 GHz RF frequency. HOM couplers are located on both sides of each cavity to extract the power lost by the beam at high current. During the experiment, the thermoionic gun delivered up to 8 mA of beam current at a pulse duration of 600 μs with bunch frequency of 216.7 MHz. The additional experimental set-up includes the following devices:

- A tuneable voltage modulator at the cathode of the gun, providing the required charge modulation along the bunch train, with a modulation amplitude nearly up to 100 % of the nominal 37 pC bunch charge.
- A 'dog-leg' magnet (half a chicane) in front of the accelerating module providing a steady horizontal offset, in the range from 0 to 20 mm.
- A broadband cavity BPM [3] to measure individual positions of the bunches located about 10 m downstream of the accelerating module exit.

Entering the module, beam energy was about 9 MeV. The gradients of the eight cavities in the module were set to a minimum value of 2 MV/m in order to maximise the sensitivity of the beam to HOM deflections. With such energy settings and quadrupole magnets off, the BPM is at a focal point for parallel trajectories entering the module. This makes it easier to measure HOM kicks in the cavities.

3 OBSERVATION OF THE 2585 MHz HOM

As discussed in [2], all HOMs can be excited by sidebands of the beam harmonics, at frequencies $nf_b \pm F$, by scanning the charge modulation frequency F through half a Brillouin zone [0, f_b/2]. Dipole modes are in principle excited by injecting the beam off-axis in the cavities. By doing so, a beam instability was observed on the broadband BPM for F = 15.022 MHz with a short beam pulse of 35 μs and 5 mA current, and a large injection offset of about 20 mm. The beam pulse length could be increased to up to 500 μs while remaining on the HOM resonance. Fig.1 shows the comparison of the BPM envelope signals with charge modulation off or on for a 400 μs long beam pulse. With modulation off, the

broadband BPM integrates a high but constant 100 mV level of beam induced noise, although the beam is steered through its centre. This is due to the rejection of the *sum* signal into the *difference* signal BPM antennas. While the modulation is on, the beam offset reaches a maximum of about 10 mm but, due to the excessive noise no quantitative measurement could be made. A damped oscillatory behaviour of the envelope signal is visible in Fig.1 with a period of about 125 μs, on top of the constant envelope of the beam oscillations reached at the steady state. This behaviour was later explained, and reproduced by simulations, by the fact that the modulation frequency was off HOM-resonance by about 8 kHz (1/125 μs). The resonant oscillations then reach a steady state after some damped overshooting. Simulations predict that for a perfectly on-resonance excitation, the oscillations reach the aperture limit within the 35 μs short pulse: this agrees with the observed veto from the beam loss protection system occurring at every attempt to fine tune the modulation frequency towards lower values of F.

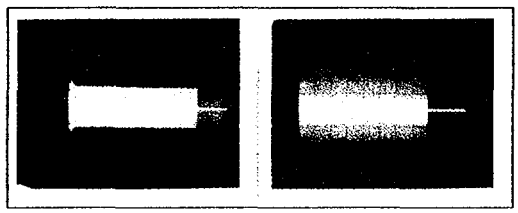

Figure 1: BPM signal on oscilloscope for 400 μs beam pulse without (left) and with (right) charge modulation

4 HOM RF CHARACTERISATION

The beam experiment revealed the existence of a HOM with a frequency $f_{HOM} = n f_b \pm$ (15.022 MHz – 8 kHz) in the accelerating module. While detuning cavities #1 and #2 had no effect on the beam instability, detuning cavity #3 by about ±16 kHz in the fundamental mode did suppress the instability. It was then possible to measure and identify the mode at the HOM coupler outputs of cavity #3 (cavity S10 in Table 1) with a spectrum analyser. The frequency domain signal around the 12th beam harmonics at 2.6 GHz in Fig.2 shows a beam modulation side-band peak enhanced by the HOM resonance on the low side of this harmonics. The same signal, when analysed in time domain in Fig.3, shows the 35 μs beam-pulse cavity loading, followed by the relaxation of the field amplitude with a characteristic time τ = 110 μs. The dipolar nature of the mode was demonstrated by checking the perfect linear dependance of the height of the amplitude maximum with the offset of the beam entering the module, over a range from 0 to 20 mm.

The resonant modes of cavity #3 were studied over a wider range of frequencies while the beam was turned off. As shown by Fig.4, the measured HOM is the highest frequency mode of the 3rd dipole passband. Its frequency is:

$$f_{HOM} = 2584.986 \text{ MHz} \pm 1 \text{ kHz}.$$

The damping factor is then given by :

$$Q = \frac{2\pi f_{HOM} W}{P_d} = \frac{2\pi f_{HOM} \tau}{2} \approx 9\times10^5$$

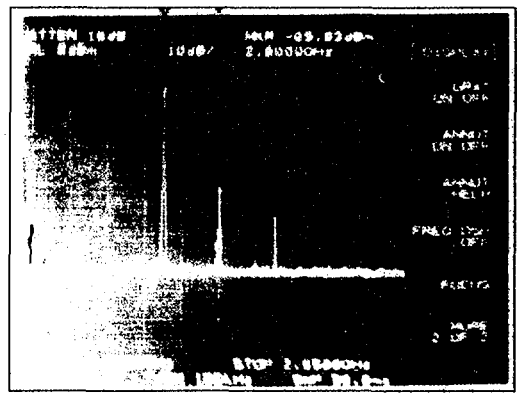

Fig.2 Sidebands around the 2.6 GHz beam harmonics

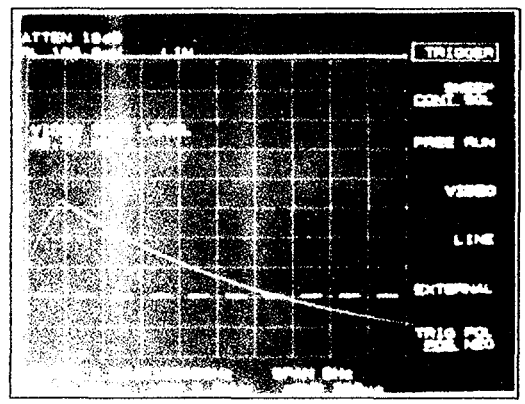

Fig.3 Time domain signal from HOM pickup on the 2585 MHz mode

An URMEL [4] calculation of the 3rd passband of the TESLA cavity was performed in parallel [5] showing that the highest frequency mode of this passband has indeed a large beam coupling impedance

$$\frac{1}{a^2}\left(\frac{R}{Q}\right) \approx 15\ \Omega/\text{cm}^2.$$

It is foreseen to compare this prediction with a quantitative measurement of the beam displacement

using a BPM with an improved resolution in a future experiment.

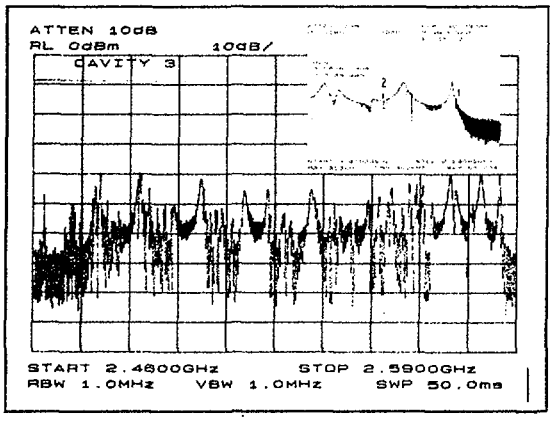

Fig.4: Third dipole passband of cavity #3. The high frequency edge of this passband is zoomed, showing the 2585 MHz (1) and 2577.5 MHz (2) very sharp modes discussed in the text.

5 OTHER MEASURED MODES

Three other modes have been excited and observed with the intensity modulated beam. The HOM excitation signal, taken either from the HOM coupler outputs or from the BPM itself, was analysed with a spectrum analyser, like in the previous section.

- 2586 MHz mode in cavity #6: a close inspection of the last mode of third dipole passband of the eight cavities (cf. Table 1) showed, in cavity #6 (S11), the same excitation curve as the one shown in Fig.3 with a time decay constant of τ = 8 μs. It corresponds to a quality factor $Q = 6.5\times10^4$. No measurable excitation could be observed in other cavities.
- 2577.5 MHz mode in cavity #3: this mode also belongs to the 3rd dipole passband, as can be seen in Fig.4. Its coupling impedance [5] is also large, about 9 Ω/cm^2. Its excitation curve gave τ = 22 μs which corresponds to $Q = 1.8\times10^5$.
- 1876 MHz mode in cavity #3: this well-known TM110 mode of the first dipole passband has a high coupling impedance of about 9 Ω/cm^2. In cavity #3, and for one polarisation, it appears to be less efficiently damped than in the other cavities [6] with a measured τ = 20 μs, corresponding to $Q = 1.2\times10^5$. This damping is at the limit of the TESLA tolerances [1].

Table 1: Cavities of TTF Module #1

Name	HOM coupler type	3rd dipole passband
D3	fixed	2458 – 2548 MHz
S8	dismountable	2458 – 2576 MHz
S10	dismountable	2471 – 2585 MHz
D1	fixed	2464 – 2562 MHz
D2	fixed	2462 – 2560 MHz
S11	dismountable	2480 – 2586 MHz
D4	fixed	2456 – 2556 MHz
S7	dismountable	2472 – 2576 MHz

6 CONCLUSION

A higher order 2585 MHz dipole mode has been observed and excited with beam with low damping, $Q = 9\times10^5$ in cavity #3 and $Q = 6.5\times10^4$ in cavity #6, in two out of eight cavities of the first TTF cryomodule. Identifying this mode with the highest mode of the third dipole passband leads to quite a high transverse coupling parameter $1/a^2 (R/Q_\perp) \cong 15$ Ω/cm^2. This is notably above the TESLA tolerance for the preservation of the vertical emittance in the linac. The origin of the insufficient damping of this mode and of its non-systematic character is not yet understood. A localised HOM coupler defect is of course one possibility. The large cavity-to-cavity spread in HOM frequencies, with highest and similar frequencies in cavities #3 and #6, may also be a clue. This observation is currently being completed by RF and beam measurements at the cold module. On the other hand, in order to complete the search of dangerous HOMs, it is foreseen to equip the new TTF photo-injector with a pockell-cell device which allows to modulate the charge of a 54 MHz bunch train.

7 REFERENCES

[1] "TESLA Conceptual Design Report", R. Brinkmann, G.Materlick, J.Rossbach and A. Wagner Editors, DESY 1997-048, (1997)

[2] "A New Method to Detect the High Impedance Dipole Modes of TESLA Cavities", S. Fartoukh, CEA/Saclay preprint, DAPNIA/SEA-98-18, (1998)

[3] "High Resolution BPM for Future Colliders", C. Magne, M. Juillard, M. Lalot, A. Mosnier, B. Phung, Y. Lussignol and R. Bossart, LINAC98 Conf., Chicago, (1998)

[4] "On the computation of resonant modes in cylindrically symmetric cavities", T. Weiland, NIM 216 (1983).

[5] We thank S. Chel for doing this calculation while the experiment was going on.

[6] G. Kreps, unpublished.

Proceedings of the 1999 Particle Accelerator Conference, New York, 1999

AN ALTERNATIVE SCHEME FOR STIFFENING SRF CAVITIES BY PLASMA SPRAYING

S.Bousson, M.Fouaidy, H.Gassot, T.Junquera, J.Lesrel, IPN Orsay, France

J.L Borne,J.Marini, LAL Orsay

C.Antoine, J.P.Charrier, H.Safa, DSM/DAPNIA/SEA CEA Saclay

Abstract

Stiffening of bulk niobium SRF cavities is mandatory for reducing the frequency shift induced by Lorentz forces at high accelerating gradients. Experimental and computational data previously reported show that with the actual scheme (i.e. EB welded stiffening rings) the frequency shift of TESLA 9 cells SRF cavities is higher than the cavity bandwidth above Eacc=28 MV/m. We propose a new stiffening method, using a Plasma Sprayed Copper Layer (PSCL) onto bulk niobium cavities. As compared to the actual technique, this method offers several advantages (simplicity, reliability...). The first experimental data obtained with monocell cavities produced by this method demonstrate the efficiency of cavities stiffening with plasma spraying. Thermal and mechanical properties measured on niobium samples with a PSCL are also presented. These data will allow us choose the plasma spraying process suitable for achieving the best cavities performances.

1 INTRODUCTION

Recent results obtained with 9-cells TESLA cavities point out a new problem for cavity stiffening. The actual EB welded stiffening rings are no more efficient for accelerating field above 28 MV/m, Lorentz forces detuning becoming too important as compared to the cavity bandwidth. As cavities recently reached 33 MV/m [1], stiffening is already a problem and a solution has to be found. A new stiffening method is proposed, based on the coating of bulk Nb cavities by a plasma sprayed copper layer. The coating must be efficient for accelerating fields up to 40 MV/m, which is the ultimate TESLA goal. Thanks to its good thermal conductivity, copper was the best material candidate to avoid cavity performances degradation. Mechanical characteristics of the copper coating could be close to bulk material with a suitable spraying process. As the Young modulus decreases strongly with the porosity, we have to find a spraying process which allows the lowest possible porosity (a few percent). Bond strength and achievable thickness are also very important issues. These properties are essential for choosing the more suitable spraying process.

2 THERMAL SPRAYING TECHNIQUES

The different thermal spraying methods can be divided into 3 different kinds [2].

a) Plasma spraying.

The principle is to create a plasma by an electric arc discharge initiated in a gas (usually Ar/H_2). The copper powder is injected in the high temperature plasma and the molten particles are sprayed out of the plasma gun. Depending on the spraying environment, different techniques were developed : under air (Atmospheric Plasma Spaying, APS), under inert gas (Controlled Atmosphere Plasma Spraying, CAPS), and under vacuum (Vacuum Plasma Spraying , VPS).

b) Combustion flame spraying.

The flame spraying (FS) principle is to use the chemical energy of combustion of fuel gas in oxygen to heat up the powder. If the oxygen is at a high pressure, the method is called High Velocity Oxy-Fuel Spraying (HVOF), and when an explosive mixture of oxygen and acetylene is used to post accelerate with the detonation (1-15 detonations per second), it is called Detonation-Gun Spraying (DGS).

c) Arc Spraying (AS).

Consumable electrodes made by two wires of the coating material are molten by arc heating, and the produced droplet is propelled by compressed gas. Some coating mechanical properties are summarised in Table 1.

Table 1: Main coating properties.

Method	porosity	bond strength	Comments
APS	medium	high	
VPS	low	high	no oxidation
CAPS	medium	high	no oxidation
FS	high	low	
DGS	low	high	pulsed
HVOF	low	high	
AS	high	low	

The first cavities were copper coated using the industrial APS method, and we are now working in a close collaboration with Ecole Nationale Superieure des Mines de Paris to improve this technique (lower porosity, higher bond strength without bonding layer). Moreover the HVOF and VPS methods are investigated with help of Institut Polytechnique de Sevenans (LERMPS, France).

3 RF TESTS ON Nb/Cu CAVITIES

In order to study the feasibility of the new fabrication method, we performed RF tests on a 1.3 GHz monocell cavity before and after the copper coating. Initially, the cavity was 2.5 mm thick, made from RRR 200 Nb sheets, and then stiffened with a 2.5 mm thick copper layer. The coating was made by a "rough APS", a not optmised process, with the use of an intermediate ≈0.2 mm thick bonding layer (bronze/aluminium alloy) between niobium and copper. The two resulting Qo vs Eacc curves (Fig.1) show only a slight reduction of the maximum attainable field (quench), while the Qo level is almost not decreased.

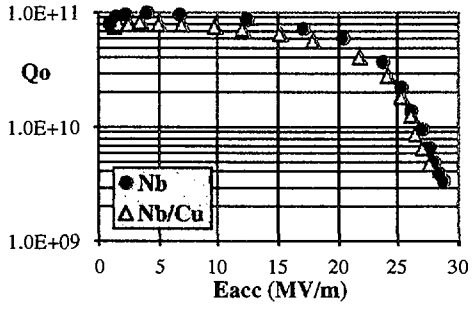

Fig. 1: Qo vs Eacc curves before and after copper coating on a 1.3 GHz monocell cavity (C1 02) @ 1.7 K.

During these experiments, the cavity frequency shift induced by Lorentz forces was measured. As theoretically expected, the frequency shift due to Lorentz forces depends quadratically on the accelerating field: $\Delta f = K.E_{acc}^2$, where K is a constant. On the Fig. 2, the 35 % decrease of the slope of Δf vs E^2_{acc} curve (Nb vs Nb with APS Cu coating) gives the stiffening efficiency of the APS copper coating.

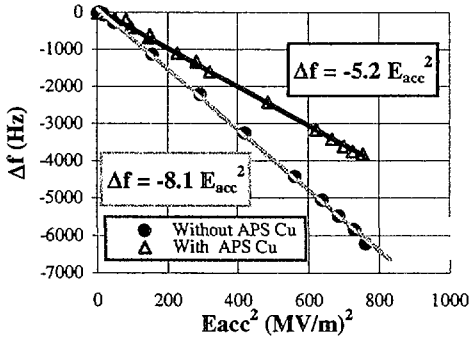

Fig 2 : Δf vs E_{acc}^2 with and without APS Cu.

To carry on the study of the new stiffening method, five 3 GHz cavities were fabricated from RRR 40 Nb sheets of 0.5 mm thickness [3]. The copper deposition process was first tested on the cavity #3, and then two more cavities (#4 and #5) were RF tested before and after Cu coating by the "rough APS" method. The results summarised in Table 2 show that the cavity performances are almost not modified by the APS Cu coating. Cavities #1 and #2 were tested before stiffening and reached high accelerating fields despite the poor Nb quality (Eacc= 24.5 MV/m for cavity #2). A study of several PS methods are currently in progress on samples in order to define the best stiffening method that will be tested on cavity #1 and #2.

Table 2: 3 GHz cavity tests @ 1.8 K.

Cavity number	E_{acc}max before Cu deposition	E_{acc}max with Cu
# 1	12.5 MV/m	to be tested
# 2	24.5 MV/m	to be tested
# 3	not tested	10 MV/m
# 4	16.5 MV/m	16 .5 MV/m
# 5	14.5 MV/m	13.5 MV/m

4 THERMAL INVESTIGATIONS

The stiffening coating adds a supplementary thermal resistance ΔRg on the overall thermal resistance (Rg) Rg=Rc+Rk+ΔRg, with Rc the conductivity term for the niobium and Rk the Kapitza resistance term (Kapitza resistance is nearly the same for Nb and Cu). Thermal simulations were performed to determine the ΔRg threshold above which the cavity thermal behaviour could be modified (either by a maximum accelerating field decrease or by an effect on the Qo level). Both defect free case and defect case were studied. On the figure 4 is plotted the defect free case theoretical Qo vs Eacc for bulk Nb (ΔRg=0). We have then calculated the Qo vs Eacc curves for an increase ΔRg of the overall thermal resistance, which is arbitrarily taken as equal to Rk and 3 Rk. These two runs simulates a possible increase of Rg due to the copper coating.

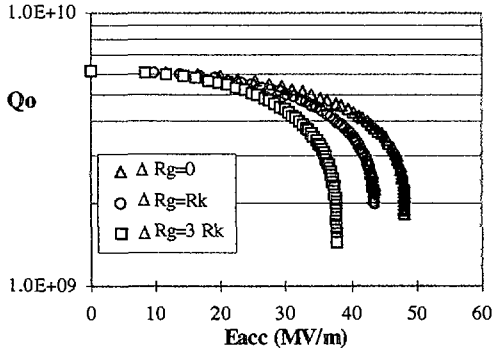

Fig. 4 : Simulation of Qo vs Eacc (defect free case) at T=2 K @ 1.3 GHz with RRR=200 and 2.5mm thick.

The results clearly show that if ΔRg=Rk (=1.4 10^{-4} $W.m^2/K$ @ 2 K), the TESLA goal (Eacc=40 MV/m)

could be achieved, whereas if ΔRg =3 Rk, this goal is not reached. The defect case study leads to the same conclusion, so a threshold on the coating thermal resistance was determined for achieving the stiffening without drawbacks at 40 MV/m.

In order to measure ΔRg due to the copper layer on our cavities, Nb samples were coated by the same "rough APS" process. ΔRg is obtained from the overall thermal resistance difference between a Nb sample and a Cu coated Nb sample [3]. At 1.8 K, ΔRg was found to be 6.4 10^{-4} Km^2/W (about 4 times Rk). In this result, the effect of the bonding layer (0.2 mm thick bronze/aluminium alloy) was suspected to dominate the thermal resistance, so another Nb sample coated with only the alloy coating was also measured. The result was the same (ΔRg =6.2 10^{-4} Km^2/W) clearly indicating the very low thermal conductivity of the bonding layer.

5 MECHANICAL SIMULATIONS

Numerical simulations have been performed to study the effect of different stiffening schemes using an additional copper layer on a TESLA 9-cells cavity detuning. The basics of the model are to consider a bimetal Nb/Cu cavity (see Fig. 5), each material considered as bulk material perfectly bonded to each other [3].

Fig.5 : Stiffened bimetal Nb/Cu cavity.

This ideal case was used to model different stiffening options, with homogeneous or non-homogeneous (thicker coating at the iris) copper layer, and Lorentz forces detuning @ Eacc = 40 MV/m was computed for TESLA 9-cells cavities. The results are reported in Table 3. They show that with the actual stiffening scheme (2.5 mm Nb thickness and EB welded stiffening rings), the frequency shift is twice the cavity bandwidth (434 Hz for Qext =3.10^6). Thanks to a non-homogeneous copper coating (2 mm thick layer and 20 mm at the iris), a frequency shift @ 40 MV/m within the cavity bandwidth was obtained.

Table 3: Computed frequency shift for TESLA cavities at Eacc = 40 MV/m for different stiffening schemes.

Configuration	Δf
niobium 2.5 mm unstiffened	-2135Hz
Nb 2.5 mm + EB welded stiffening rings	**-863 Hz**
Nb 2.5 mm + Cu coating 2 mm	-883 Hz
Nb 2.5 mm + Cu coating 2 mm + iris stiffening (h=20mm)	**-358 Hz**

The Young modulus of the coating used with the 3 GHz cavity prototypes was estimated to 27 GPa from a simple experiment which consists in measuring the coated cavity deformation versus the applied axial force and comparison with a model calculation. Using this value, simulations on 9-cells TESLA cavities give a Δf of 616 Hz at 40 MV/m (non-homogeneous scheme), a value higher than the cavity bandwidth, but still an improvement as compared to the 863 Hz obtained with the actual EB welded stiffening rings. Simulations also show that this coating is efficient for accelerating fields up to 33 MV/m. Different theoretical approaches modelled the effect of the porosity on the Young modulus. As the bulk copper Young modulus is 130 GPa, the estimated value (27 GPa) is in the range of expected values of APS coating with porosity lying between 15% and 30%. Mechanical model calculations show that to achieved an effective stiffening at 40 MV/m, it is necessary to have a coating Young modulus of 95 GPa, which corresponds to a porosity of a few percent.

6 CONCLUSION AND FUTURE

A new fabrication method for SRF cavities is presented. The principle is to stiffen niobium cavities with a copper layer deposited by thermal spraying. Comparison of RF performances obtained with the first cavities tested before and after copper deposition showed that the maximum accelerating field was not affected, while a stiffening effect was measured. These results demonstrate the interest of the method. But this "rough APS" copper coating is efficent only for Eacc < 33 MV/m. Mechanical simulations have proved that porosity have to be less than a few percent. Thermal measurements showed that for this coating at 40 MV/m, the cavity thermal stability should not be affected if the bonding layer is removed.

This first study pointed out the important parameters involved in the cavity stiffening. Now, a new program has just started to investigate other spraying process (VPS, HVOF, and a more controlled APS), more suited to our application. After measurements of mechanical and thermal properties on samples, 3 GHz and 1.3 GHz cavities will be fabricated from 1 mm thick Nb sheets of RRR 130 and then stiffened with the copper layer.

7 ACKNOWLEDGMENTS

The authors would like to thank M.Boloré, A.Caruette, J.Y.Gasser, N.Hamoudi, A.Le Goff, J.C.Le Scornet, J.P.Poupeau, for their technical assistance and helpful discussions. They would like also to thank C.Coddet, C.Verdy (LERMPS) and V.Guipont, M.Jeandin (Ecole des Mines) for collaborating on plasma spraying.

8 REFERENCES

[1] W.D.Möller "The performance of the 1.3 GHz superconducting RF cavities in the first module of the T.T.F linac" linac98, Chicago (1998).

[2] Lech Pawlowski " The Science and Engineering of Thermal Spray Coating " J.Wiley & sons.

[3] M.Fouaidy et al. And reference here cited, " A New Fabrication and Stiffening Method of SRF Cavities " EPAC'98, Stockholm.(1998).

A LASER TRIGGERED ELECTRON SOURCE FOR PULSED RADIOLYSIS

H. Monard#, J.C. Bourdon, J. Le Duff, T. Garvey, B. Mouton, J. Rodier,Y. Thiery,
Laboratoire de l'Accélérateur Linéaire, Université de Paris-Sud, IN2P3 - CNRS, Orsay, France.
M. Gaillard,
Laboratoire de Photophysique Moléculaire, Université de Paris-Sud, IN2P3 - CNRS, Orsay, France.

Abstract

We present the design of a photo-injector based accelerator for pulsed radiolysis applications. This machine is destined to meet the needs of the physical chemistry community at the Université de Paris XI. A 4 MeV electron pulse of a few picoseconds duration and with a charge in the range of 1 to 10 nC is produced from a Cs_2-Te photocathode. The photocathode is placed in the half cell of a 1-1/2 cell, 3 GHz RF gun, whose design is based on the gun used for the drive beam of the CERN CLIC Test facilty. A 4 cell "booster" cavity is then used to accelerate the beam to an energy of 9 MeV. The transport system consists of a quadrupole triplet downsteam of the booster, two rectangular, 30 degree bend, dipoles with a pair of quadrupoles between them and a second triplet downstream of the second dipole. Energy dependent path length effects in the two dipoles allow the possibilty of magnetic bunch compression depending on the phase-energy correlation of the bunch exiting the booster cavity. The beam envelope and the bunch length have been calculated through the transport line using TRACE-3d and PARMELA. These codes allow us to verify the required beam parameters at the experimental areas. We will discuss the adjustment of the optics, aimed at producing the minimum electron bunch length at the experimental targets.

1 INTRODUCTION

The project ELYSE aims to provide the physical chemistry community with a tool to study rapid chemical reaction dynamics. Chemical samples will be irradiated by a fast, high charge electron pulse and the resulting reactions will be analysed using a laser pulse synchronised with the electron beam. The necessity for both a laser and electron beam to perform such 'pump-probe' experiments suggests the use of a photoinjector for the electron beam, as the laser to be used as a probe can also be employed to produce the electron beam. The beam requirements necessary for ELYSE are given in table 1. Although the nominal charge per bunch is set to 1 nC one hopes to be able to produce more intense pulses (up to 10 nC) with similar pulse widths. In addition to these conditions there is a need to reduce the charge from the dark current arriving at the experimental samples to a level of < 1% of the charge of the primary beam. As the RF pulse width is of the order of 3 μs the dark current must not exceed a few microamperes.

Table 1: ELYSE beam specifications

Energy	4 - 9 MeV
Bunch charge	> 1 nC
Bunch duration	< 5 ps (FWHM)
Energy spread	< 2.5 % (RMS)
Normalised emittance	< 60 mm-mr (RMS)
Beam size on target	2 - 20 mm

2 THE ACCELERATOR

The layout of the accelerator, chosen to satisfy the ELYSE requirements, is shown in figure 1.

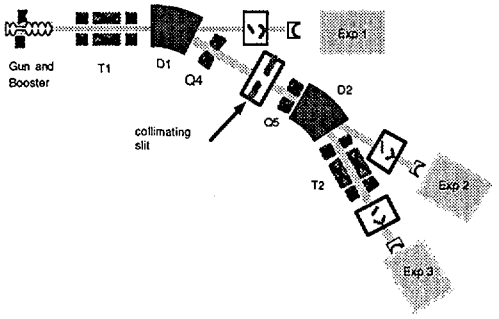

Figure 1. The accelerator layout.

It consists of a 1-1/2 cell RF gun, followed by a four cell "booster" cavity and a magnetic transport line to deliver the beam to one of three experimental areas (EA). The choice of the gun is based on the design used at CERN for the CLIC Test Facility [1]. The 1-1/2 cell gun will provide a beam of approximately 4 MeV while the booster cavity will allow further acceleration to 9 MeV. A solenoidal magnet is placed at the exit of the gun to focus the beam through the booster. The design of the transport line is chosen with two objectives in mind. The use of the two dipoles allows the dark current from the source to be filtered out before arriving at EA2 or EA3. If necessary, the collimating slit can further reduce the dark current but at the expense of losses in the primary beam. Secondly, the correlated phase-energy dependence of the

Email : monard@lal.in2p3.fr

beam leaving the booster can be exploited to provide temporal compression of the bunches due to energy dependent path length effects in the transport line [2]. This will help to compensate space-charge effects which will tend to lengthen the pulse duration, particularly on EA1.

3 SIMULATIONS

2.1 The electron gun

As stated above, the electron gun is based on the design used at the CTF. Nevertheless, we have made slight modifications to allow operation of the gun at lower cathode gradients (65 MV/m) with the aim of reducing the dark current while still allowing transport of the high charge through the booster. Optimisation of the gun was performed with SUPERFISH. The calculated field distribution was then used as input for PARMELA calculations of the beam envelope. The magnetic field of the solenoid was calculated with POISSON.

2.2 The transport line

The design and calculated settings of the transport line were made bearing in mind that the most important parameter, for the experimental targets is the bunch length. The layout of the line is rather classical. The beam exiting the booster encounters a first quadrupole triplet followed by two dipoles with a pair of quadrupoles between them and, finally, a second triplet. The machine has a point of symmetry centered between the pair of quadrupoles. This means that the dipoles, quadrupoles and triplets are identical as are the lengths of the corresponding drift spaces

The RMS beam parameters at the exit of the booster, calculated using PARMELA, were used to provide input Twiss parameters for TRACE-3d in each of the phase spaces (x,x'), (y,y') and (ϕ,E). TRACE-3d has the advantage of allowing quadrupole fitting procedures and permits one to quickly check on the transport. On the other hand, only the linear part of the space charge field is taken into account. For this reason, we used PARMELA to calculate the envelope through the entire machine with the quadrupole settings found using TRACE-3d. No major discrepancies are seen when comparing the transverse RMS beam enlevopes. However, the final bunch length calculated with PARMELA appears to be slightly longer than that calculated with TRACE-3d. The difference may be due to the inclusion of the non-linear space charge fields when using PARMELA.

Now let us discuss the transport setting from the exit of the booster up to EA3. The phase space co-ordinates at the exit of the transport line, x_i, are related to those at the entrance, x_{0j},by the transfer matrix R_{ij} using the equation,

$$X_i = \sum_{j=1}^{6} R_{ij} X_{0j} \qquad (i = 1,2,...,6),$$

where $x_i \equiv (x, x', y, y', \delta z, \delta p/p)$. First, we find the correct settings for the pair of quadrupoles (Q4 and Q5) in order to have the transport matrix elements $R_{51} = R_{52} = 0$. This setting makes the bunch compression independent of the geometric terms at the exit of the booster cavity. Moreover, it is also the correct setting for a first-order achromatic transport (neglecting space charge effects). The fields of the first triplet are then adjusted to give a reasonable value for the horizontal beam size between the two dipoles. Finally, the second triplet is set to deliver the required beam size, at EA3. It is then necessary to re-adjust Q4 and Q5 to maintain $R_{51} = R_{52} = 0$. If the gun and booster are adjusted to provide the required phase-energy correlation then bunch length compression occurs after the beam traverses the two dipoles.

2.3 The dipoles

The dipoles were designed with the 2D-codes POISSON and OPERA [3]. We have chosen to use rectangular, C-type magnets, with a 30° bend angle, and a bending radius of 500 mm. The main windings were calculated to produce a maximum magnetic field of 0.1 T. A secondary winding allows one to cancel remanent fields of the order of 20 G, in order to deliver the beam to experimental areas 1 & 2 when required.

2.4 Results

The initial conditions for the PARMELA calculation assume an RMS laser pulse, σ_τ = 1ps, truncated at ± 2.5 σ_τ. Figure 2 shows the phase-energy correlation at the exit of the booster for a 1 nC beam at 9 MeV. Even for the highest charge and lowest energies of interest, the beam exiting the booster meets the user requirements.

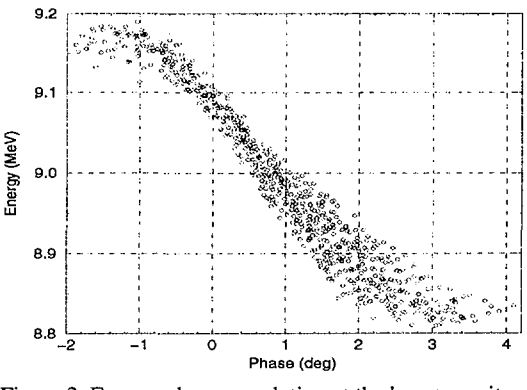

Figure 2. Energy-phase correlation at the booster exit.

The envelope of the same beam transported from the booster exit to EA3 is shown in figure 3. The calculated bunch compression in this case is 28% although we have shown that 50% can be achieved. At 9 MeV and 1 nC the

desired pulse length is obtained (see Table 2, figure 3). At the lower energy of 4 MeV we still manage to transport 1 nC to EA3 but we see that the space charge effects lead to a longer pulse.

Table 2. Parameters at EA3 for 1 nC charge.

Energy	4 MeV	9 MeV
σ_τ	3.7 ps	0.8 ps
$\delta E/E$	3.6%	2.3%
RMS norm. emitt.	51 mm-mr	70 mm-mr

In contrast, we note that the charge of 10 nC cannot be transported without some loss in the second dipole. We continue to perform calculations to optimise the transmission at 10 nC.

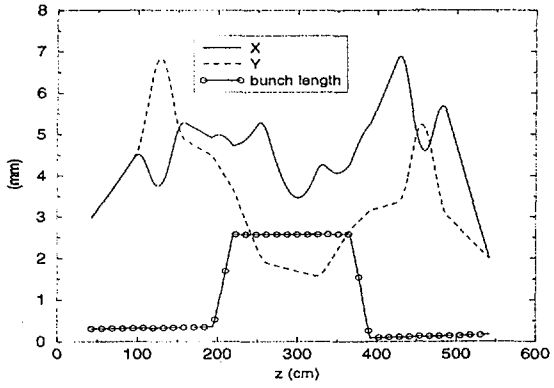

Fig. 3. The RMS values of the transverse and longitudinal dimensions of the beam through the transport line as calculated using TRACE-3d.

4 THE PREPARATION CHAMBER

As we aim to extract high charges (~ 10 nC) with a laser energy of ~ 50 μJ at 266 nm we choose to use a caesium-telluride photocathode. These cathodes, as well as having a high quantum efficiency (>1%), are now known to have a long lifetime, of the order one month [4] and exhibit low dark current [1]. However, the choice of such a cathode requires the use of a dedicated preparation chamber. We plan to install a simplified preparation chamber based on the design of a new chamber currently being installed at CERN for the CLIC Test Facilty probe beam [4].

5 PROJECT STATUS

In this paper we have mainly discussed the simulation work aimed at verifying that the desired beam performance can be obtained. In parallel with these calculations we have been making progress on the construction of the machine. Low level measurements have been performed on a prototype RF gun to fix the dimensions of the gun. We will use a booster structure which already exists. The entire RF network for feeding the gun and booster has been ordered from industry as has the klystron. The modulator will be built in-house. The quadrupoles and solenoid are under construction in industry and the dipoles are out to tender. Once delivered they will be tested using the facilities at LURE. The magnet power supplies will also be built by a group from the LURE laboratory. Position and intensity instrumentation is being developed at LAL. The control system has been contracted to industry and is well in progress. The vacuum system has been designed and many components are already on site with others ordered. The LAL drawing office is working on the design of many of the mechanical components (vacuum chambers, diagnostic ports, supports etc..). ELYSE will use an entirely commercial laser which has already been delivered.

The facility will be housed in an existing building which is currently being renovated. Installation and 'first beam' are foreseen for the summer of the year 2000.

6 ACKNOWLEDGEMENTS

We are pleased to acknowledge the aid of R. Bossart and J.C. Godot of CERN for helpful discussions on the RF gun as well as G. Suberluqc (CERN) for advice on the preparation chamber. We thank M. Corlier (LURE) for assistance in the specification of all the magnetic elements of ELYSE, and in particular for her aid in the dipole calculations. Finally, we thank H. Borie (LAL) for the preparation of the technical specifications for ELYSE components. Funding for ELYSE is provided by the CNRS, the MENRT, the Université de Paris-Sud, the Conseil Regional Ile-de-France and the Conseil General de l'Essone.

7 REFERENCES

[1] R. Bossart et al., "Modular electron gun consisting of two RF sections and an intermediate focusing solenoid", Nucl. Inst. and Meth. A, Vol 340, pp 157-163 (1994)

[2] M. Uesaka et al., "Precise measurements of a sub-picosecond electron single bunch by the femtosecond streak camera", Nucl. Inst. and Meth. A, Vol 406, pp 371-379 (1998).

[3] H. Monard, "Etude des Dipôles pour l'accélérateur d'ELYSE", Internal Report, LAL/SERA, 99-30 (1999).

[4] E. Chevallay et al., "Photocathodes for the CERN CLIC Test Facility", Proceedings of The 19th International Linear Accelerator Conference (Chicago), 1998.

A CURE FOR THE ENERGY SPREAD INCREASING RELATED BUNCH LENGTHENING IN ELECTRON STORAGE RINGS

J. Gao, LAL, B.P. 34, F-91898 Orsay cedex, France

Abstract

Having revealed the cause of the energy spread increasing and the corresponding bunch lengthening in electron storage rings in ref. 1, in this paper, we will propose a cure for the suppression of these collective effects. It is suggested to install an active rf cavity in the ring with the working rf wavelength about four to five times the rms bunch length. The limitation about this cure is also discussed. Finally, in the postscript, we will give an empirical bunch lengthening equation and compare the analytical results with some experimental results.

1 INTRODUCTION

In modern electron colliders, such as B and Tau-C Factories, short bunch lengths are required in order to get high luminosities. In practice, the bunch length will suffer from two kinds of lengthening effects. The first one is due to the potential well distortion and the second is due to the so-called collective random excitation (CRE) revealed in ref. 1. According to ref. 1 one has two equations for the energy spread increasing ($\mathbf{R}_\varepsilon = \sigma_\varepsilon/\sigma_{\varepsilon 0}$) and the bunch lengthening ($\mathbf{R}_z = \sigma_z/\sigma_{z_0}$)

$$\mathbf{R}_\varepsilon^2 = 1 + \frac{\mathcal{C}(R_{av}RI_b\mathcal{K}_{||,0}^{\rm tot})^2}{\gamma^7\mathbf{R}_z^{2.42}} \qquad (1)$$

$$\mathbf{R}_z^2 = 1 + \frac{C_{PWD}I_b}{\mathbf{R}_z^{1.5}} + \frac{\mathcal{C}(R_{av}RI_b\mathcal{K}_{||,0}^{\rm tot})^2}{\gamma^7\mathbf{R}_z^{2.42}} \qquad (2)$$

where

$$\mathcal{C} = \frac{576\pi^2\epsilon_0}{55\sqrt{3}\hbar c^3} \qquad (3)$$

ϵ_0 is the permittivity in vacuum, $\hbar$ is Planck constant, c is the velocity of light, $I_b = eN_ec/2\pi R_{av}$, R_{av} is the average radius of the ring, R is the bending radius, $\mathcal{K}_{||,0}^{\rm tot}$ is the total longitudinal loss factor at the zero current bunch length, C_{PWD} represents potential well distortion effect, N_e is the electron number in a bunch, and γ is the normalized particle energy.

In this paper we will investigate the possibility to suppress the CRE induced bunch energy spread increasing and the corresponding bunch lengthening.

2 CURE: INTRODUCING AN ACTIVE RF CAVITY IN THE RING

A bunch of N_e particles inside will has a definite short range wake potential profile corresponding to its charge distribution. What should be stressed is that for a given bunch current even the longitudinal position of each electron inside the bunch is a random variable, the collective wake potential profile remains stable. As shown in ref. 1, after each turn an electron will get a net kick on its energy by

$$\Delta E_i = \mathcal{U}_w \sin(\Omega_s t - \phi_i) \qquad (4)$$

where ϕ_i is a random variable, Ω_s is the angular synchrotron oscillation frequency, and $\mathcal{U}_w = e^2N_e\mathcal{K}_{||}^{\rm tot}(\sigma_z)$ is the average single particle energy loss due to short range wakefield per turn. It is these random energy fluctuations which are responsible for the bunch energy spread increasing. The idea to suppress these kicks is to create an artificial counteract kicks $-eV_0sin(\Omega_s t-\phi_i)$. Since it is known that an electron will get maximum positive kicks at the very head and the tail of the bunch, and the maximum negative kick near the middle of the bunch as shown in Fig. 1a, one can use a standing wave rf cavity with the wavelength of the working mode (with rf input power) about four to five times the rms bunch length. The phase relation of this mode with respect to the passing bunch should be arranged as follows: The head and the tail gets the maximum energy reduction by $-eV_0$ each turn and the middle of the bunch gets the maximum energy gain eV_0 per turn as shown in Fig. 1b (in a practical point of view, the phase shift should be adjustable to adapt different shape of wake potentials). Obviously, to cancel the collective random kicks one has to choose $V_0 = \mathcal{U}_w/e$ which is the peak voltage gain of an electron passing through the cavity. The required rf input power can be easily obtained by

$$P_0 = V_0^2/R_{sh} \qquad (5)$$

where R_{sh} is the shunt impedance of the standing wave rf cavity. Once this is done, eqs. 1 and 2 will be changed to

$$\mathbf{R}_\varepsilon^2 \approx 1 \qquad (6)$$

$$\mathbf{R}_z^2 \approx 1 + \frac{C_{PWD}^*I_b}{\mathbf{R}_z^{1.5}} \qquad (7)$$

where $|C_{PWD}^*| > |C_{PWD}|$ due to the additional impedance contribution from the rf cavity. Till now the CRE induced energy spreading increasing and the related bunch lengthening effects have been suppressed.

As a natural rule one has to pay for what he gains, and this time it is the transverse instability.

3 LIMITATION COMING FROM THE TRANSVERSE INSTABILITY

Here, we will make a quick review of the single bunch transverse instability in electron storage rings. The threshold bunch current for the transverse instability derived in

ref. 2 is expressed as:

$$I_{b.gao}^{th} = \frac{4 f_y \sigma_{\varepsilon 0} \mathbf{R}_\varepsilon |\xi_{c,y}|}{e < \beta_{y,c} > \mathcal{K}_\perp^{tot}(\sigma_z)} \quad (8)$$

where ν_y is the vertical betatron oscillation tune, respectively, $< \beta_{y,c} >$ is the average beta function in the rf cavity region, $\xi_{c,y}$ is the chromaticity in the vertical plane (usually positive to control the head-tail instability), and $\mathcal{K}_\perp^{tot}(\sigma_z)$ is the total transverse loss factor over one turn. This threshold current indicates the disappearance of Landau damping. On the other hand, the usually used Zotter's formula coming from the mode coupling theory gives

$$I_{b.zotter}^{th} = \frac{F f_s E_0}{e < \beta_{y,c} > \mathcal{K}_\perp^{tot}(\sigma_z)} \quad (9)$$

where F is variable depending on bunch length, f_s is the synchrotron oscillation frequency, and E_0 is the particle energy. To compare eq. 8 with eq. 9 one can write eq. 8 in a similar form as eq. 9

$$I_{b.gao}^{th} = \frac{F' f_s E_0}{e < \beta_{y,c} > \mathcal{K}_\perp^{tot}(\sigma_z)} \quad (10)$$

with

$$F' = 4 \mathbf{R}_\varepsilon |\xi_{c,y}| \frac{\nu_y \sigma_{\varepsilon 0}}{\nu_s E_0} \quad (11)$$

where ν_s is the synchrotron oscillation tune. Apparently, if $F' < F$, $I_{b,gao}^{th} < I_{b.zotter}^{th}$ and this situation can always be realized experimentally by reducing $|\xi_{c,y}|$. If, however, eq. 9 and eq. 10 describe the same physical process, one finds the explicit expression of F ($F = F'$).

The impact of the longitudinal motion on that of the transverse one can be perceived by finding $\mathbf{R}_\varepsilon$ and σ_z in eq. 8. Obviously, better longitudinal bunch properties (smaller energy spread and shorter bunch length) result in lower transverse instability threshold current.

4 DISCUSSION

Recent experiments on super-ACO [4] show that by using negative momentum compaction factor α one can get shorter bunch length, and unfortunately, larger energy spread compared with positive α case. This result is easily understood by looking at eqs. 1 and 2. With negative α, C_{PWD} becomes negative, and in consequence, one gets smaller $\mathbf{R}_z$ and larger $\mathbf{R}_\varepsilon$. Now, if one uses the additional active rf cavity proposed in section 2, eqs. 1 and 2 are reduced to eqs. 6 and 7. Obviously, $\mathbf{R}_z$ and $\mathbf{R}_\varepsilon$ are decoupled from each other, and hopefully, one can get at the same time smaller energy spread and shorter bunch length. As far as the rf cavity design is concerned, one should manage to avoid the cavity beam pipe being excessively small. The detailed discussion on the cavity design will be made after the cure principle shown in this paper be justified by the numerical simulations.

5 CONCLUSION

An additional active rf cavity is proposed to be installed in the ring to suppress the collective random excitation induced energy spread increasing and the corresponding bunch lengthening. The wavelength of the working mode should be four to five times the rms bunch length. One should be cautious to the transverse instability since smaller energy spread and shorter bunch length will result in lower transverse instability threshold current. It could be interesting to use this technique together with negative momentum compaction factor to obtain short bunch with small energy spread.

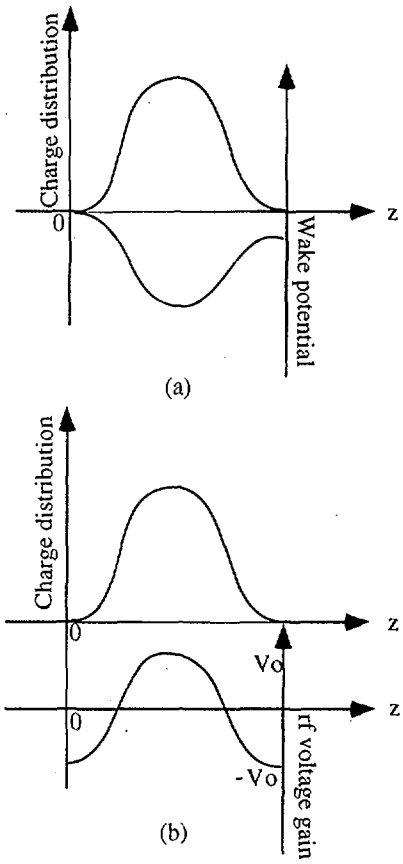

Figure 1: (a) Schematic showing of the bunch charge distribution and the short range wake potential. (b) Schematic showing of the rf voltage gain with respect to the particle position within the bunch.

6 POSTSCRIPT

Here, exceptionally, we add a section of "postscript" where an empirical bunch lengthening equation is given as:

$$\mathbf{R}_z^2 = 1 + \frac{\sqrt{2\mathcal{C}} R_{av} R K_{||,0}^{\mathrm{tot}} I_b}{\gamma^{3.5} \mathbf{R}_z^{1.21}} + \frac{\mathcal{C}(R_{av} R I_b K_{||,0}^{\mathrm{tot}})^2}{\gamma^7 \mathbf{R}_z^{2.42}} \quad (12)$$

An interesting property of this formula is that $K_{||,0}^{tot}$ plays a unique dominating role. The reason for my calling this equation as empirical is because the second term on the right side of eq. 12 is not derived on a theoretical base. In Figs. 2 to 6 we make the comparison between the analytical and the experimental results of different machines. More detailed explications and comparison results can be found in ref. 5

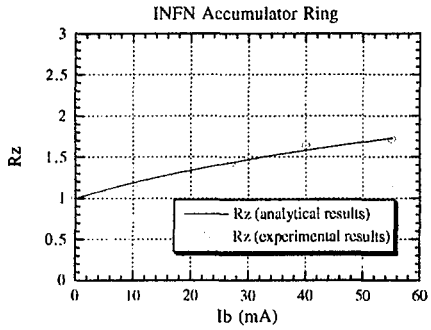

Figure 2: Comparison between INFN (R = 1.15 m and R_{av} = 5 m) experimental results and the analytical results at 510 MeV with σ_{z_0}=3.57 cm and $K_{||,0}^{tot}$=0.39 V/pC.

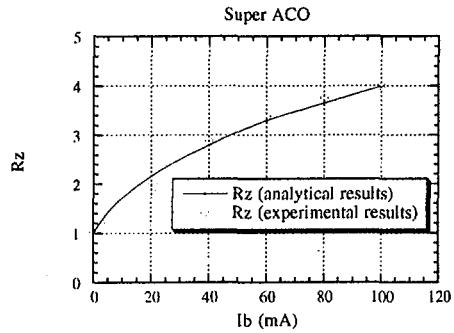

Figure 3: Comparison between Super-ACO (R = 1.7 m and R_{av} = 11.5 m) experimental results and the analytical results at 800 MeV with σ_{z_0}=2.4 cm and $K_{||,0}^{tot}$=3.1 V/pC.

7 REFERENCES

[1] J. Gao, "Bunch lengthening and energy spread increasing in electron storage rings", *Nucl. Instr. and Methods*, A**418** (1998), p. 332.

[2] J. Gao, "Theory of single bunch transverse collective instabilities in electron storage rings", *Nucl. Instr. and Methods*, A**416** (1998), p. 186.

[3] B. Zotter, LEP note 363 (1982).

[4] A. Nadji, P. Brunelle, G. Flynn, M.-P. Level, M. Sommer, H. Zyngier, "Experiments with low and negative momentum compaction factor with super-ACO", Proceedings of EPAC96, Barcelona, Spain, 1996.

[5] J. Gao, "An empirical equation for bunch lengthening in electron storage rings", to be published.

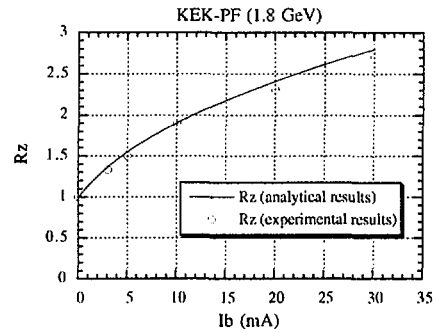

Figure 4: Comparison between KEK-PF (R = 8.66 m and R_{av} = 29.8 m) experimental results and the analytical results at 1.8 GeV with σ_{z_0}=1.47 cm and $K_{||,0}^{tot}$=5.4 V/pC.

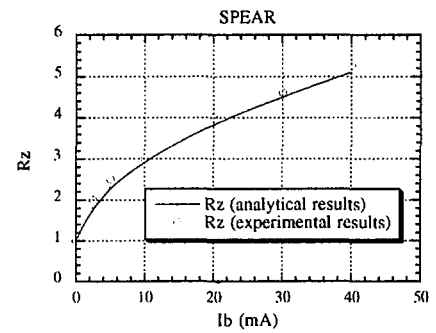

Figure 5: Comparison between SPEAR (R = 12.7 m and R_{av} = 37.3 m) experimental results and the analytical results at 1.5 GeV with σ_{z_0}=1 cm and $K_{||,0}^{tot}$=5.2 V/pC.

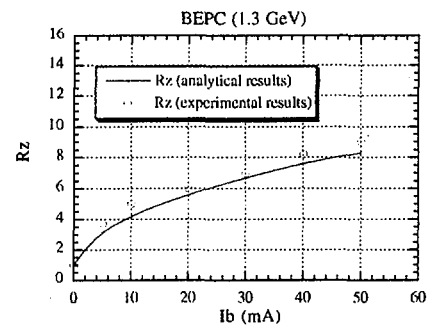

Figure 6: Comparison between BEPC (1.3 GeV) (R = 10.345 m and R_{av} = 38.2 m) experimental results and the analytical results at 1.3 GeV with σ_{z_0}=1 cm and $K_{||,0}^{tot}$=9.6 V/pC.

Proceedings of the 1999 Particle Accelerator Conference, New York, 1999

SINGLE BUNCH LONGITUDINAL INSTABILITIES IN PROTON STORAGE RINGS

J. Gao, LAL, B.P. 34, F-91898 Orsay cedex, France

Abstract

In this paper we try to explain the single bunch energy spread increasing in a proton storage ring. Different from an electron machine, the random motions of some particles of a bunch are caused by the nonlinear synchrotron oscillations perturbed by the short range longitudinal wakefield. An analytical single bunch threshold current formula has been established to indicate the beginning of the longitudinal random motions. By using kinetic descriptions one shows that the energy spread of the particles which execute random motions will increase, and the energy spectrum width of the random motions will be enlarged with increasing bunch current.

1 INTRODUCTION

The problem of the longitudinal instabilities in a proton storage ring is quite different from that in an electron one where the synchrotron radiation plays an important role [1]. It is observed experimentally that below an apparent threshold bunch current the bunch length increases with increasing current while the bunch energy spread remain unchanged, and the mechanism of this bunch lengthening is explained quite well by the potential well distortion theory. When the bunch current surpasses the threshold value the energy spread of the bunch increases also. In this paper, we try to explain the mechanism of the single bunch energy spread increasing in a proton storage ring and establish an analytical formula for the threshold current.

2 LONGITUDINAL MOTION PERTURBED BY SHORT RANGE WAKEFIELD

In a circular proton storage ring a non-synchronous particle will oscillate around the the synchronous one under the rf focusing in the longitudinal direction, and its phase ϕ with respect to the rf accelerating potential is determined by the following differential equation [2]:

$$\frac{d^2\phi}{dt^2} + \frac{\Omega_s^2}{\cos\phi_s}(\sin\phi - \sin\phi_s) = 0 \tag{1}$$

and

$$\Omega_s^2 = \frac{e\hat{V}h\eta\omega_s\cos\phi_s}{2\pi R_s p_s} \tag{2}$$

where $\hat{V}$ is the peak accelerating voltage, h is the harmonic number, $\eta = 1/\gamma^2 - \alpha$, γ is the normalized particle energy, α is the momentum, R_s is the average radius of the ring, $\omega_s = c/R_s$, p_s and ϕ_s are the momentum and the phase of the synchronous particle. For the convenience in the later mathematical treatment, we approximate eq. 1 by the following differential equation

$$\frac{d^2\Delta\phi}{dt^2} + \Omega_s^2\sin\Delta\phi = 0 \tag{3}$$

where $\Delta\phi = \phi - \phi_s$. For the stationary bucket eq. 1 and eq. 3 are equivalent. It is obvious that $\Delta\phi$ oscillates as a pendulum. The deviation of a particle with respect to the synchronous one in terms of energy is expressed as follows:

$$\Delta E = -\frac{R_s p_s}{h\eta}\frac{d\Delta\phi}{dt} \tag{4}$$

By defining $P = \frac{d\Delta\phi}{dt}$ and $Q = \Delta\phi$, eq. 3 can be derived from an Hamiltonian $H(Q, P, t)$ expressed as

$$H(Q, P, t) = \frac{1}{2}P^2 - \Omega^2\cos Q \tag{5}$$

where P and Q are canonical. Let us change P and Q to the action-angle variables, I and θ. By introducing two variables ($\tilde{N}$ and ξ)

$$\tilde{N}^2 = \frac{1}{2}(1 + \frac{H}{\Omega_s^2}) \tag{6}$$

and

$$\tilde{N}\sin\xi = \sin\frac{Q}{2}, (\tilde{N} \le 1) \tag{7}$$

one gets [3]

$$I(H) = \frac{8}{\pi}\Omega_s\left(E(\frac{\pi}{2};\tilde{N}) - (1-\tilde{N}^2)F(\frac{\pi}{2};\tilde{N})\right), (\tilde{N} \le 1) \tag{8}$$

$$\theta = \frac{\partial S(Q, I)}{\partial I} \tag{9}$$

with

$$S(Q, I) = 4\Omega_s\left(E(\xi;\tilde{N}) - (1-\tilde{N}^2)F(\xi;\tilde{N})\right), (\tilde{N} \le 1) \tag{10}$$

where $F(\xi;\tilde{N})$ and $E(\xi;\tilde{N})$ are the first and second kind elliptical integrals, respectively. The frequency of this nonlinear oscillator can be obtained easily as

$$\Omega(H) = \frac{dH(I)}{dI} = \frac{\pi\Omega_s}{2F(\frac{\pi}{2};\tilde{N})}, (\tilde{N} \le 1) \tag{11}$$

It is obvious that on the separatrix ($\tilde{N} = 1$) one has $H = H_c = \Omega_s^2$, and $\Omega(H_c) = 0$. Due to the interaction between the charged particles and the environment, after each turn a bunch will loss energy $W = e^2N_p^2\mathcal{K}_{//}^{tot}(\sigma_z)$, where N_p is the number of particles in the bunch, $\mathcal{K}_{//}^{tot}(\sigma_z)$ is the total longitudinal loss factor of one turn, and σ_z is the bunch

length (here we assume that particles are relativistic, otherwise, $\mathcal{K}_{//}^{tot}(\sigma_z)$ will depend on the particle velocity, and space charge forces should be taken into account). This energy loss will be compensated by the rf cavities. Since the short range longitudinal wakefield varies within the bunch and the synchrotron oscillation period is much longer than that of one revolution, the additional energy variation of a particle due to the short range wakefield after each turn can be reasonably expressed as

$$dE = \mathcal{U}_w \cos\theta = e^2 N_p \mathcal{K}_{//}^{tot}(\sigma_z)\cos\theta \qquad (12)$$

Obviously, averaging over one synchrotron period one has $< dE >= 0$. Taking into account this additional energy variation after each revolution and the fact that this happens at instants t_k with constant interval T_0 (T_0 is the revolution period), a new Hamiltonian can be represented in the form:

$$H(I,\theta,t)^* = H(I) + \frac{1}{2}\Delta P^2 T_0 \sum_{k=-\infty}^{\infty}\delta(t-kT_0)$$

$$= H(I) + \frac{(dE)^2 h^2\eta^2}{2R_s^2 p_s^2} T_0 \sum_{k=-\infty}^{\infty}\delta(t-kT_0)$$

$$= H(I) + \frac{\mathcal{U}_w^2 h^2\eta^2\cos^2\theta}{2R_s^2 p_s^2} T_0 \sum_{k=-\infty}^{\infty}\delta(t-kT_0) \qquad (13)$$

where we have omitted the crossing term coming from eq. 4 and eq. 12 since both quantities are statistically independent. Eq. 13 can be simplified as

$$H(I,\theta,t)^* = H(I) + \Delta H T_0 \sum_{k=-\infty}^{\infty}\delta(t-kT_0)$$

$$= H(I) + \frac{\mathcal{U}_w^2 h^2\eta^2\cos 2\theta}{4R_s^2 p_s^2} T_0 \sum_{k=-\infty}^{\infty}\delta(t-kT_0) \qquad (14)$$

where a constant term has been dropped, and

$$\Delta H = \Delta H_0 \cos 2\theta = \frac{\mathcal{U}_w^2 h^2\eta^2}{4R_s^2 p_s^2}\cos 2\theta \qquad (15)$$

Consequently, one has

$$\frac{dI}{dt} = -\frac{\partial \Delta H}{\partial\theta} T_0 \sum_{k=-\infty}^{\infty}\delta(t-kT_0) \qquad (16)$$

$$\frac{d\theta}{dt} = \Omega(I) + \frac{\partial \Delta H}{\partial I} T_0 \sum_{k=-\infty}^{\infty}\delta(t-kT_0) \qquad (17)$$

Since the kicks on the pendulum $H(I)$ repeat after constant time interval T_0, and between the kicks the motion is known, one can replace eqs. 16 and 17 by a so-called *universal mapping*:

$$I_{n+1} = I_n - T_0\frac{\partial \Delta H}{\partial\theta} \qquad (18)$$

$$\theta_{n+1} = \theta_n + \Omega_s T_0 + \Omega' I_{n+1} T_0 \qquad (19)$$

where $\Omega' = d\Omega/dI$. We transform then the universal mapping into *standard mapping* which is expressed as

$$J_{n+1} = J_n + K_0 \sin\Psi \qquad (20)$$

$$\Psi_{n+1} = \Psi_n + J_{n+1} \qquad (21)$$

where $\Psi = 2\theta$, $J = 2T_0\Omega' I$, $K_0 = 4\Omega' T_0^2 \Delta H_0$, and a constant term has been omitted from eq. 21. At this stage we can discuss the condition on which there starts to have chaotic motions. To this end we can use the Chirikov criterion [4] which shows that when

$$|K_0| \geq 1(0.97) \qquad (22)$$

the Kolmogorov-Arnold-Moser (KAM) invariant tori will be broken and the particles which satisfy this condition will move in a *random* way. From eq. 22 one gets the threshold bunch current of the onset of the stochastic motion

$$I_{b,th} = \frac{R_s p_s}{e\sqrt{|\Omega'| T_0^2 h|\eta|\mathcal{K}_{//}^{tot}(\sigma_z)}} \qquad (23)$$

Taking advantage of our simplifying the longitudinal motion of a particle to a pendulum, we can have the analytical expression for Ω'. When a particle moves near the separatrix, one gets

$$|\Omega'| = \frac{1}{\pi^4|1 - H_b/H_c|}\left(\ln\frac{32}{|1-H_b/H_c|}\right)^3 \qquad (24)$$

where

$$\frac{H_b}{H_c} = \left(\frac{\delta E_b}{\delta E_{max}}\right)^2 = \frac{\pi h|\eta| E_s}{\beta^2 e\dot{V} G(\phi_s)}(\delta E_b)^2 \qquad (25)$$

$$G(\phi_s) = 2\cos\phi_s - (\pi - 2\phi_s)\sin\phi_s \qquad (26)$$

H_b and δE_b are the maximum Hamiltonian value and the relative energy spread of the bunch, δE_{max} is the maximum acceptance of the rf bucket in terms of relative energy spread, β and E_s are the normalized velocity and the energy of the particle, respectively.

3 ENERGY SPREAD INCREASING

For those particles which have already executed chaotic motions a kinetic description of them will be appropriate. We will loss, certainly, some detailed information on the particle trajectories, this method, however, will help us to get useful physical results. When the random motion occurs eqs. 20 and 21 can be regarded as a Markov process, and in consequence, the possibility distribution function $F(t, I)$ is described by the Fokker-Planck equation:

$$\frac{\partial F}{\partial t} = -\frac{\partial(\mathcal{A}F)}{\partial I} + \frac{1}{2}\frac{\partial^2(\mathcal{D}F)}{\partial I^2} \qquad (27)$$

where $\mathcal{A}$ and $\mathcal{D}$ are defined as follows:

$$\mathcal{A} = \frac{1}{2\pi T}\int_0^{2\pi}\Delta I d\theta \qquad (28)$$

$$\mathcal{D} = \frac{1}{2\pi T}\int_0^{2\pi} \Delta I^2 d\theta \tag{29}$$

where T is a small time interval. The legitimation of making average over the phase θ is based on the fact that the particle which moves randomly will mix its phase in the phase space. For our specific case described by eqs. 18 and 19 with $T = T_0$, one has

$$\mathcal{A} = 0 \tag{30}$$

$$\mathcal{D} = \frac{e^2 N_p^2 \mathcal{K}_{//}^{tot}(\sigma_z)^2 h^2 \eta^2}{2R_s^2 p_s^2} T_0 \tag{31}$$

Putting $\mathcal{A} = 0$ and $\mathcal{D}$ into eq. 27, one gets

$$\frac{\partial F}{\partial t} = \frac{1}{2}\mathcal{D}\frac{\partial^2 F}{\partial I^2} \tag{32}$$

From eq. 32, one finds that stochastic heating occurs in the following way:

$$< I^2 >= I_0^2 + \mathcal{D}t \tag{33}$$

where $< I^2 >= \int_0^\infty I^2 F dI$. Similarly, one finds

$$< \Delta E^2 >= \Delta E_0^2 + \mathcal{D}_e t \tag{34}$$

$$\mathcal{D}_e = \frac{\mathcal{U}_w^2}{2T_0} \tag{35}$$

Obviously, the amplitude of the energy deviations of those particles executing random motions will increase with time. From eq. 35 it is evident that the resistive part of the impedance of the machine determines the diffusion coefficient instead of the reactive part. The relevant effect of the interaction between the charged particles with the reactive part impedance is the potential well distortion which results in the reduction of the area of the rf bucket.

The distinction between an electron and a proton storage rings is that there exists always a stable (cold) core in the bunch of proton particles around the synchrotron particle where no energy spread increasing occurs.

4 THE POWER SPECTRUM OF THE RANDOM MOTIONS

As shown in section 2, when the bunch current surpasses the threshold current $I_{b,th}$, some particles in the bunch will execute random motions, and the longitudinal positions of these particles will be random variables. When $I_b \gg I_{b,th}$, the autocorrelator of these random motion has the form [3]

$$\mathcal{R}(t) = \mathcal{R}_0 \exp\left(-\frac{t}{\tau_c}\right) \tag{36}$$

$$\tau_c = \frac{2T_0}{\ln K_0} = \frac{T_0}{\ln\left(\frac{\sqrt{\Omega'}T_0 e^2 N_p \mathcal{K}_{//}^{tot}(\sigma_z)h\eta}{R_s p_s}\right)} \tag{37}$$

By virtue of Wiener-Khintchine theorem, we know that the spectral power density of the random variable is the Fourier transform of its autocorrelation function, and we have then

$$S(\omega) = \frac{1}{2\pi}\int_{-\infty}^{\infty} \exp(i\omega t)\mathcal{R}(t)dt = \frac{1}{\pi}\mathcal{R}_0 \frac{\tau_c}{1+\omega^2\tau_c^2} \tag{38}$$

The power spectrum $S(\omega)$ falls off rapidly when

$$\omega > \omega_c = \frac{1}{\tau_c} \tag{39}$$

The variation of ω_c with respect to the bunch current can be measured experimentally, and apparently, one has $\omega_c \propto \ln(I_b)$.

5 DISCUSSION ON THE BUNCH LENGTHENING

In a proton machine, a bunch suffers from potential well distortion induced bunch lengthening just like what happens in an electron storage ring. When $I_b \geq I_{b,th}$ some particles in the bunch will execute random motions and the synchrotron oscillation amplitudes of these particles will increase (but not those of the particles in the stable core). In a global point of view, the bunch length increases much more quickly with respect to the increasing bunch current compared with when $I_b < I_{b,th}$. Since not all particles participate the random motions, it is much more difficult to get some simple formulae or equations to describe the global bunch lengthening and the energy spread increasing for the whole bunch current range as what has been done in ref. 1 for the electron storage rings.

6 CONCLUSION

In a proton storage ring, it is shown that the nonlinear longitudinal motion perturbed by the short range longitudinal wakefield can change the regular synchrotron motions of some particles in a bunch into random ones. An analytical formula of the threshold current for the onset of the random motion is established. The particles which execute random motions will be heated and their energy spread will increase. The width of the energy spectrum of the random motions is proportional to $\ln I_b$.

7 REFERENCES

[1] J. Gao, "Bunch lengthening and energy spread increasing in electron storage rings", *Nucl. Instr. and Methods*, A**418** (1998), p. 332.

[2] J. Le Duff, CERN 85-19, p. 125.

[3] R.Z. Sagdeev, D.A. Usikov, and G.M. Zaslavsky, "Nonlinear physics from the pendulum to turbulences and chaos", Contemporary conceptes in physics, harwood academic publishers, 1988.

[4] B. Chirikov, Phys. Reports, Vol. 52, No. 5 (1979), p. 263-379.

Proceedings of the 1999 Particle Accelerator Conference, New York, 1999

ANALYTICAL INVESTIGATION ON THE HALO FORMATION IN SPACE CHARGE DOMINATED BEAMS

J. Gao, LAL, B.P. 34, F-91898 Orsay cedex, France

Abstract

It is assumed that Fermion particles, such as electron and proton, in a matched beam follow Fermi-Dirac statistics in the equilibrium state. Parametric resonances, chaotic motion, and halo formation in transverse direction of motion are investigated analytically. The analytical expressions for the parametric resonances and the maximum transverse position deviation, above which chaotic motion starts to occur due to transverse beam envelope oscillation, are derived. Analytical formula for the current loss rate is established.

1 INTRODUCTION

Recently, high power ion beams are more and more demanded in the related possible applications such as thermonuclear energy production, transmutation of radioactive wastes, the production of tritium and the special materials, and the conversion of plutonium. One of the major challenges on the linac is to keep the machine maintenance hand-accessible which can be roughly quantified by a rule-of-thumb of the average particle loss rate < 1 nA/GeV/m [1]. The lost particles are mainly from the halo which surrounds the beam core. Among others, the particle-core model proposed by O'Connell, Wangler, Mills, and Crandall [2] is the simplest and the most explored, which illustrates many important features of the dynamics of the particles which constitute the halo with the assumption that the core has a uniform density and zero emittance. A good summary of what we know about the halo formation in linacs is given in ref. 3. The problem with the existing models, however, is that it is not obvious to predict the particle loss rate. In this paper we try to explain analytically the halo formation processes in detail, and try to estimate the halo current loss rate analytically.

2 PARTICLE DENSITY DISTRIBUTION

Kapchinskij and Vladimirskij derived the envelope and single particle transverse motion differential equations for a continuous beam as follows (we limit ourselves to round and continuous beams) [4]:

- Envelope equation:

$$\frac{d^2R}{dz^2} + \omega_0^2 R - \frac{K}{R} - \frac{\epsilon^2}{R^3} = 0 \qquad (1)$$

where R is the beam envelope in a continuous solenoid focusing channel, $K = 2(I_b/I_0)/(\beta\gamma)^3$, $\pi\epsilon$ is the beam unnormalized transverse emittance, γ and β are the normalized particle's energy and velocity (v/c), respectively, I_b is the beam current, and $I_0 = 4\pi\epsilon_0\pi m_0 c^3/q$ with m_0/q being the mass charge ratio of the particle ($I_0 = 3.1 \times 10^7$ A for proton).

- Single particle equations:

$$\frac{d^2x}{dz^2} + \left(\omega_0^2 - \frac{K}{R^2}\right) x = 0 \qquad (2)$$

when $x < R$, and

$$\frac{d^2x}{dz^2} + \omega_0^2 x - \frac{K}{x} = 0 \qquad (3)$$

when $x > R$. Since the KV envelope equation is derived from a specific microcanonical distribution, the validity for the other kinds of distribution is not automatic. According to Lapostolle [5] and Sacherer [6], one can use the same form of envelope equation for any possible particle distributions provided that the envelope and the emittance are defined as

$$R^2 = 4\overline{x^2} \qquad (4)$$

$$\epsilon = 4\sqrt{\overline{x^2x'^2} - \overline{xx'}^2} \qquad (5)$$

From now on the form of the envelope equation expressed in eq. 1 is regarded as particle density distribution independent. Now we distinguish two cases: the matched and mismatched beams. Considering now a continuous focusing channel, for the first case one means:

$$\omega_0^2 R - \frac{K}{R} - \frac{\epsilon^2}{R^3} = 0 \qquad (6)$$

and

$$\frac{d^2x}{dz^2} + \omega_p^2 x = 0 \qquad (7)$$

for $x < R$, where $\omega_p^2 = \epsilon^2/R^4$. For the matched case, apparently, when $\epsilon = 0$ the motions of particles within the beam envelope can be equivalent to those of particles in collision free gas of zero temperature (in this paper we consider only Fermion gas such as electron and proton which have half-integral spins). For the zero emittance matched beam envelope radius, R_0, one finds $R_0 = \sqrt{K}/\omega_0$. When $\epsilon \neq 0$ the stationary envelope radius will become $R = R_0 + \delta R$. Putting this expression into eq. 1, for $\delta R << R$, one finds

$$\delta R = \frac{\epsilon^2}{2\omega_0^2 R_0^3} \qquad (8)$$

From eq. 1 one knows that if R deviate a little bit from R_0 at zero emittance limit the envelope oscillates approximately like an harmonic oscillator:

$$\frac{d^2\delta R}{dz^2} + \omega_R^2 \delta R = 0 \qquad (9)$$

where $\omega_R = \sqrt{2}\omega_0$ which is called the envelope oscillation frequency. Now we are at the stage to estimate the equilibrium particle density distribution function, $n(x)$. As noted above we regard the particles in the matched beam as the particles in a Fermion gas, and in consequence, the density distribution follows Fermi-Dirac statistics:

$$n(E) = \frac{n_{E=0}}{1+\exp\left((E-\mu)/kT\right)} \tag{10}$$

where E is the particle's transverse oscillation energy, μ is the chemical energy of the gas, k is the Boltzmann constant, and T is the temperature of the gas. The transverse oscillation energy of a particle is proportional to the square of its plasma oscillation amplitude and kT is proportional to the square of Debye length, λ_D. One rewrites eq. 10 as

$$n(x) = \frac{n_{x=0}}{1+\exp\left((x^2-R_0^2)/\lambda_D^2\right)} \tag{11}$$

where λ_D is estimated as follows:

$$\lambda_D^2 = \frac{v_{thermal}^2}{\omega_p^2} = \frac{\delta R^2\omega_R^2}{\omega_p^2} = \frac{1}{2}\frac{\epsilon^2}{\omega_0^2 R_0^2} \tag{12}$$

or

$$\frac{\lambda_D}{R_0} = \frac{\omega_p}{\omega_R} \tag{13}$$

Now we look at a more general situation when the beam is not matched with $R = R_0 + \Delta R$ and $\Delta R << R_0$. In analogy with δR we know that ΔR oscillates with envelope frequency, ω_R also. In the equilibrium state (there is no diffusion process exists) particles are assumed to follow Fermi-Dirac statistics as in the case of matched beam. The general expression for λ_D is obtained as:

$$\lambda_D^2 = \frac{v_{thermal}^2}{\omega_p^2} = \frac{(\delta R^2 + \Delta R^2)\omega_R^2}{\omega_{\Delta R}^2 + \omega_p^2} \tag{14}$$

where $\omega_{\Delta R}^2 = 2\omega_0^2\Delta R/R_0$, ΔR and δR are statistically independent. When $\Delta R = 0$ eq. 14 reduces to eq. 12. In the case where the contribution from the definite emittance can be neglected eq. 14 can be simplified as:

$$\left(\frac{\lambda_D}{R_0}\right)^2 \approx \frac{\Delta R}{R_0} \tag{15}$$

To study single particle dynamics we assume that for $x < R_0 - \lambda_D$ and $x > R_0 - \lambda_D$ the particle transverse motions are described by eqs. 2 and 3, respectively.

3 INSTABILITY DUE TO PARAMETRIC RESONANCE: ARNOL'D TONGUES

In this section a mismatched beam in a continuous focusing channel is considered since for a matched periodic focusing channel the procedure to treat the problem is the same. From eq. 2 it is found that if the beam envelope is modulated from the matched radius, R_0, by $\Delta R_c(z)$, the differential equation of motion reads:

$$\frac{d^2x}{dz^2} + \left(\omega_p^2 + \frac{2K}{R_0^3}\Delta R_c(z)\right)x = 0 \tag{16}$$

where $\Delta R_c(z) = \Delta R_c(z + L_c)$, and L_c is the envelope modulation period. If $\Delta R_c(z)$ is expressed as a sinusoidal function of longitudinal position, z, the stability region of x will be determined by Mathieu equation. Not sticking to the mathematic rigor we assume that $\Delta R_c(z)$ is approximated by: $\Delta R_c(z) = \Delta R_{c0}$ when $0 \le z < L_c/2$ and $\Delta R_c(z) = -\Delta R_{c0}$ when $L_c/2 \le z < L_c$. Defining

$$\omega_p' = \frac{L_c}{2\pi}\omega_p \tag{17}$$

and

$$\varpi = \left(\frac{L_c}{2\pi}\right)^2 \frac{2K\Delta R_{c0}}{R_0^3} \tag{18}$$

one gets the stable and the parametric resonance regions described by the functions [7]:

$$\omega_p' \approx n \pm \frac{\varpi^2}{\sqrt{8}n^3}, n = 1, 2, 3, \cdots \tag{19}$$

and

$$\omega_p' \approx k/2 \pm \frac{2\sqrt{2}\varpi}{\pi k^2}, k = 1, 3, 5, \cdots \tag{20}$$

For $k = 1$ we obtain the result obtained by Gluckstern [8] that when the particle frequency is about one half the core frequency the parametric resonance occurs. In this paper we generalize this particular conclusion to a more general one: *when the particle frequency is about an integer times one half the core frequency the parametric resonance occurs.*

4 THE ONSET OF HALO DUE TO NONLINEAR RESONANCES AND STOCHASTIC MOTIONS

As we have assumed in section 2 the trajectory of a particle located in the nonuniform density region is determined by eq. 3. If we define $x = R_0 + \Delta x$, where $\Delta x \ll R_0$, one finds Δx satisfies the following nonlinear differential equation:

$$\frac{d^2\Delta x}{dz^2} + \omega_0^2\Delta x + \frac{K}{R_0}\Delta x - \frac{K}{R_0}\left(\left(\frac{\Delta x}{R_0}\right)^2 - \left(\frac{\Delta x}{R_0}\right)^3 + \left(\frac{\Delta x}{R_0}\right)^4 - \cdots\right) = 0 \tag{21}$$

It has been shown numerically that the solution of Δx is stable and periodical [2]. Now let's consider the case when there is an envelope modulation, ΔR, around R_0 due to either periodic focusing or mismatching. The differential equation governing the particle motion near R_0 turns out to be:

$$\frac{d^2\Delta x}{dz^2} + \omega_0^2\Delta x + \frac{K}{R_0}\Delta x - \frac{K}{R_0}\left(\left(\frac{\Delta x}{R_0}\right)^2 - \left(\frac{\Delta x}{R_0}\right)^3 + \cdots\right) + \frac{K\Delta R}{R_0^2}\left(\frac{\Delta x}{R_0}\right)^2 - \cdots = 0 \tag{22}$$

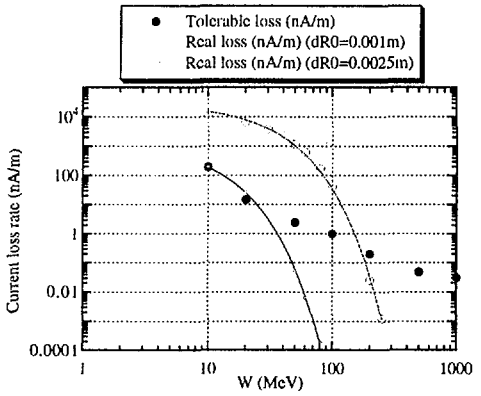

Figure 1: The current loss rates vs the energy of a proton beam of $I_b = 1$A, $R_0 = 0.005$m, $R_m = 10R_0$, $f = 0.1$, $L = 5$m, and $\beta(z) = 8$m.

For the matched case ΔR_{match} has the same period as that of the periodic focusing lattice, L. In this section we discuss only the matched periodic focusing channel, and denote $\Delta R_{match} = \Delta R_0$. To simplify the mathematics treatments we assume that $\Delta R_0(z)$ is represented by a periodic delta function of period L and amplitude ΔR_0. It is shown (see ref. 10) that under the periodic envelope oscillation perturbation if the amplitude of a particle's deviation Δx is larger than some limit, say Δx_{max}, the motion of this particle will become chaotic, and Δx_{max} is analytically expressed as follows [10]:

$$\Delta x_{max} = \left(\frac{16 R_0^8}{9 L^2 K^2 \Delta R_0 \beta(z)^2} \right)^{1/3} \qquad (23)$$

where $\beta(z)$ is the beta function of the focusing channel.

5 ESTIMATION OF BEAM CURRENT LOSS RATE

According to the discussion given above one knows that the particles located near R_0 ($x = R_0 + \Delta x$) with $\Delta x \geq \Delta x_{max}$ will diffuse outwards into the focusing-dominated region and contribute to the halo.

Now we discuss the average beam loss rate on the mechanical boundary of the beam transport system, and we may make a rough estimation in the following way. It is known that the particles located in $\Delta x \geq \Delta x_{max}$ will diffuse outwards, and the current, I_d, which participates this diffusion process can be calculated as:

$$I_d = \frac{I_b}{R_0^2} \int_{x=R_0+\Delta x_{max}}^{x=\infty} \frac{1}{1 + \exp\left(\frac{x^2 - R_0^2}{\lambda_D^2}\right)} dx^2 \qquad (24)$$

One can imagine that a uniform halo disk is formed around the beam core started from $x = R_0 + \Delta x_{max}$. Due to the beam envelope oscillation the dimension of the disk, which extends to the radius, R_m, of the mechanical aperture of the transport system, oscillates with $x = R_m \pm \Delta R_0$. Obviously, the particles located in $R_m \leq x \leq R_m + \Delta R_0$ are lost, and this loss will be filled through the diffusion process. If the particle re-distribution distance, or the so-called relaxation distance $\lambda_p/4$, ($\lambda_p = 2\pi R_0/\sqrt{3K}$) [3], is shorter than the envelope oscillation period, the beam current loss rate, $\mathcal{R}$(A/m), can be estimated as the $\mathcal{R} = I_d(\Delta R_0/R_m)^2/L$, where $R_m >> R_0$. If, however, the relaxation distance is longer than L, one has $\mathcal{R} = 4I_d(\Delta R_0/R_m)^2/\lambda_p$. To summarize, we give a simplified beam current loss rate formula as follows:

$$\mathcal{R} \approx I_b f \frac{\Delta R_0^3}{\mathcal{L} R_0 R_m^2} \ln\left(\frac{1 + \exp(2\Delta x_{max}/\Delta R_0)}{\exp(2\Delta x_{max}/\Delta R_0)} \right) \qquad (25)$$

where $\mathcal{L} = L$ when $L \geq \lambda_p/4$, $\mathcal{L} = \lambda_p$ when $L \leq \lambda_p/4$, and f is the ratio of the average beam current with respect to the peak bunch current. In Fig. 1 we give an example to show how one can use eqs. 23 and 25 to estimate the current loss and how this current loss varies with beam parameters, where we choose $R_0 = 0.005$m, $I_b = 1$A, $f = 0.1$, $L = 5$m, $\beta(z) = 8$m, $\Delta R_0 = 0.0025$m and $\Delta R_0 = 0.001$m, respectively. In the figure the tolerable current loss rate [9] is presented by the dark dots, and it is obvious that in this case ΔR_0 should be less than 0.001m.

6 CONCLUSION

It is assumed that at the equilibrium state the transverse beam density distribution of a matched beam follows Fermi-Dirac statistics (for Fermion particles). The conditions for the particles' transverse motions to have parametric resonances and nonlinear force induced stochastic motions are derived analytically. Finally, the analytical loss rate formula is established.

7 ACKNOWLEDGEMENTS

The author thanks J. Le Duff and N. Pichoff (Saclay) for the clarifying discussions and their critical comments.

8 REFERENCES

[1] R.A. Jameson, PAC93 (1993), p. 3926.

[2] J.S. O'Connell, et al., PAC93 (1993), p. 3657.

[3] T. Wangler, "*Principles of rf linear accelerators*", John Wiley and Sons, Inc. (1998).

[4] I. Kapchinskij and V. Vladimirskij, Proceedings of the II Int. Conf. on High Energy Accel. CERN 1959, p. 274.

[5] P.M. Lapostolle, Proceedings of the VII international conference on high energy accelerators, August (1969), p. 205.

[6] F.J. Sacherer, *IEEE Trans. Nucl. Sci.* **18** (1971) 1105.

[7] J.L. McCauley, *Physica Scripta*, **T20** (1988).

[8] R. Gluckstern, *Phys. Rev. Letters*, **73** (1994) 1247.

[9] A.P. Fedotov and B.P. Murin, Proceedings of the 1976 Linear Accelerator Conference, p. 377.

[10] J. Gao, LAL/RT 98-04, 1998.

Proceedings of the 1999 Particle Accelerator Conference, New York, 1999

ANALYTICAL INVESTIGATION ON THE DYNAMIC APERTURES OF CIRCULAR ACCELERATORS

J. Gao, LAL, B.P. 34, F-91898 Orsay cedex, France

Abstract

In this paper by considering delta function sextupole and octupole perturbations and using difference action-angle variable equations, analytical formulae for the dynamic aperture of circular accelerators are derived based on the Chirikov criterion of the onset of stochastic motions.

1 INTRODUCTION

One of the preoccupations of the circular accelerator designers is to estimate the influence of nonlinear forces on the single particle's motion. Even though the nonlinear forces compared with the linear ones are usually very small, what is observed in reality, however, is that when the amplitudes of the transverse oscillation of a particle are large enough, the transverse motions might become unstable and the particle itself will finally be lost on the vacuum chamber. In the following sections we will show how the nonlinear forces limit the dynamic apertures and what is the relation between them.

2 DYNAMIC APERTURES DUE TO NONLINEAR RESONANCES AND STOCHASTIC MOTIONS

In this section a necessary distinction will be made between two essentially different cases: a proton machine and an electron one. The reason is simple. In the first case there is no dissipative forces (which is generally true) and the particle's motion can be described in the frame of Hamiltonian system. In the second case, however, one has to take into account of the synchrotron radiation damping effect.

2.1 *Proton storage ring*

To start with we consider the linear horizontal motion of a particle assuming that the magnetic field is only transverse and there are no screw fields. The Hamiltonian can be expressed as

$$H = \frac{p^2}{2} + \frac{K(s)}{2}x^2 \tag{1}$$

where x denotes normal plane coordinate, $p = dx/ds$, and $K(s)$ is a periodic function satisfying the relation

$$K(s) = K(s+L) \tag{2}$$

where L is the circumference of the ring. The solution of the deviation, x, is found to be

$$x = \sqrt{\epsilon_x \beta_x(s)}\cos(\phi(s) + \phi_0) \tag{3}$$

where

$$\phi(s) = \int_0^s \frac{ds}{\beta_x(s)} \tag{4}$$

As an essential step towards further discussion on the motions under nonlinear perturbation forces, we introduce action-angle variables and the Hamiltonian expressed in these new variables [1]:

$$\Psi = \int_0^s \frac{ds'}{\beta_x(s')} + \phi_0 \tag{5}$$

$$J = \frac{\epsilon_x}{2} = \frac{1}{2\beta_x(s)}\left(x^2 + \left(\beta_x(s)x' - \frac{\beta_x' x}{2}\right)^2\right) \tag{6}$$

$$H(J,\Psi) = \frac{J}{\beta_x(s)} \tag{7}$$

Since the $H(J,\Psi) = J/\beta_x(s)$ is still a function of the independent variable, s, we will make another canonical transformation to freeze the new Hamiltonian:

$$\Psi_1 = \Psi + \frac{2\pi\nu}{L} - \int_0^s \frac{ds'}{\beta_x(s')} \tag{8}$$

$$J_1 = J \tag{9}$$

$$H_1 = \frac{2\pi\nu}{L}J_1 \tag{10}$$

Before going on further, let's remember the relation between the last action-angle variables and the particle deviation x:

$$x = \sqrt{2J_1\beta_x(s)}\cos\left(\Psi_1 - \frac{2\pi\nu}{L}s + \int_0^s \frac{ds'}{\beta_x(s')}\right) \tag{11}$$

Having well prepared we start our journey to find out the limitations of the nonlinear forces on the stability of the particle's motion. To facilitate the analytical treatment of this complicated problem we consider at this stage only sextupoles and octupoles (no screw terms) and assume that the contributions from the sextupoles and octupoles in a ring can be made equivalent to a point sextupole and a point octupole. The perturbed Hamiltonian can be thus expressed:

$$\mathcal{H} = \frac{p^2}{2} + \frac{K(s)}{2}x^2 + \frac{1}{3!B\rho}\frac{\partial^2 B_z}{\partial x^2}x^3 L\sum_{k=-\infty}^{\infty}\delta(s-kL)$$

$$+\frac{1}{4!B\rho}\frac{\partial^3 B_z}{\partial x^3}x^4 L\sum_{k=-\infty}^{\infty}\delta(s-kL) \tag{12}$$

where ρ is the radius of curvature. Representing eq. 12 by action-angle variables (J_1 and Ψ_1), and using

$$B_z = B_0(1 + xb_1 + x^2 b_2 + x^3 b_3) \tag{13}$$

one has

$$H = \frac{2\pi\nu}{L}J_1 + \frac{(2J_1\beta_x(s_1))^{3/2}}{3\rho}b_2 L\cos^3\Psi_1 \sum_{k=-\infty}^{\infty}\delta(s-kL)$$

$$+\frac{(J_1\beta_x(s_2))^2}{\rho}b_3 L\cos^4\Psi_1 \sum_{k=-\infty}^{\infty}\delta(s-kL) \quad (14)$$

where s_1 and s_2 are just used to differentiate the locations of the sextupole and the octupole perturbations. By virtue of Hamiltonian one gets the differential equations for Ψ_1 and J_1

$$\frac{dJ_1}{ds} = -\frac{\partial\mathcal{H}}{\partial\Psi_1} \quad (15)$$

$$\frac{d\Psi_1}{ds} = \frac{\partial\mathcal{H}}{\partial J_1} \quad (16)$$

$$\frac{dJ_1}{ds} = -\frac{(2J_1\beta_x(s_1))^{3/2}}{3\rho}b_2 L\frac{d\cos^3\Psi_1}{d\Psi_1}\sum_{k=-\infty}^{\infty}\delta(s-kL)$$

$$-\frac{(J_1\beta_x(s_2))^2}{\rho}b_3 L\frac{d\cos^4\Psi_1}{d\Psi_1}\sum_{k=-\infty}^{\infty}\delta(s-kL) \quad (17)$$

$$\frac{d\Psi_1}{ds} = \frac{2\pi\nu}{L} + \frac{2\beta_x^2(s_2)}{\rho}J_1 b_3 L\cos^4\Psi_1 \sum_{k=-\infty}^{\infty}\delta(s-kL)$$

$$+\frac{\sqrt{2}J_1^{1/2}\beta_x(s_1)^{3/2}}{\rho}b_2 L\cos^3\Psi_1 \sum_{k=-\infty}^{\infty}\delta(s-kL) \quad (18)$$

Now it is the moment to change this differential equations to the difference equations which is *suitable* to analyse the possibilities of the onset of stochasticity [2][3]. Since the perturbations have a natural periodicity of L we will sample the dynamic quantities at a sequence of s_i with constant interval L assuming that the characteristic time between two consecutive adiabatic invariance breakdown intervals is shorter than L/c. The differential equations in eqs. 17 and 18 are reduced to

$$\overline{J_1} = \overline{J_1}(\Psi_1, J_1) \quad (19)$$

$$\overline{\Psi_1} = \overline{\Psi_1}(\Psi_1, J_1) \quad (20)$$

where the bar stands for the next sampled value after the corresponding unbared previous value, or explicitly,

$$\overline{J_1} = J_1 - \frac{(2J_1\beta_x(s_1))^{3/2}}{3\rho}b_2 L\frac{d\cos^3\Psi_1}{d\Psi_1}$$

$$-\frac{(J_1\beta_x(s_2))^2}{\rho}b_3 L\frac{d\cos^4\Psi_1}{d\Psi_1} \quad (21)$$

$$\overline{\Psi_1} = \Psi_1 + 2\pi\nu + \frac{\sqrt{2}\beta_x(s_1)^{3/2}\overline{J_1}^{1/2}}{\rho}b_2 L\cos^3\Psi_1$$

$$+\frac{2\beta_x(s_2)^2}{\rho}\overline{J_1}b_3 L\cos^4\Psi_1 \quad (22)$$

Eqs. 21 and 22 are the basic difference equations to study the nonlinear resonance and the onset of stochasticities considering sextupole and octupole perturbations. By using trigonometric relation

$$\cos^m\theta\cos n\theta = 2^{-m}\sum_{r=0}^{m}\frac{m!}{(m-r)!r!}\cos(n-m+2r)\theta \quad (23)$$

one has

$$\cos^3\theta = \frac{2}{2^3}(\cos 3\theta + 3\cos\theta) \quad (24)$$

$$\cos^4\theta = \frac{1}{2^4}(\cos 4\theta + 4\cos 2\theta + \frac{4!}{((4/2)!)^2}) \quad (25)$$

Apparently, the right hand sides of eqs. 21 and 22 contain sinusoidal functions of phases, Ψ_1, $2\Psi_1$, $3\Psi_1$, and $4\Psi_1$. If the tune ν is far from the resonance lines $\nu = m/n$, where m and n are integers (n=1, 2, 3, and 4 for this specific problem), the invariant tori of the unperturbed motion are preserved under the presence of the small perturbations by virtue of the Kolmogorov-Arnold-Moser (KAM) theorem. If, however, ν is close to the above mentioned resonance line, the situation is getting complicated and under some conditions the KAM invariant tori can be broken. Taking the third order resonance, $m/3$, for example, we keep only the sinusoidal function with phase $3\Psi_1$ in eq. 21 and the dominant phase independent nonlinear term in eq. 22, and as the result, we have eqs. 21 and 22 reduced to

$$\overline{J_1} = J_1 + A\sin 3\Psi_1 \quad (26)$$

$$\overline{\Psi_1} = \Psi_1 + B\overline{J_1} \quad (27)$$

with

$$A = \frac{(J_1\beta_x(s_1))^{3/2}}{\sqrt{2}\rho}b_2 L \quad (28)$$

$$B = \frac{3\beta_x(s_2)^2}{4\rho}b_3 L \quad (29)$$

where we have dropped the constant phase in eq. 22. It is helpful to transform eqs. 28 and 29 into the form so-called *standard mapping* [3] expressed as

$$\overline{I} = I + K_0\sin\theta \quad (30)$$

$$\overline{\theta} = \theta + \overline{I} \quad (31)$$

with $\theta = 3\Psi$, $I = 3BJ_1$ and $K_0 = 3AB$. By virtue of the Chirikov criterion [3] it is known that when $|K_0| \geq 0.97164$ [4] stochastic motions will appear and the diffusion will occur. Therefore,

$$|K_0| \leq 1 \quad (32)$$

can be taken as a natural criterion for the determination of the dynamic aperture of the machine. Putting eqs. 28 and 29 into eq. 32, one gets

$$|K_0| = \frac{9}{4\sqrt{2}}|b_2 b_3|\beta_x^2(s_2)\beta_x^{3/2}(s_1)J_1^{3/2}\frac{L^2}{\rho^2} \leq 1 \quad (33)$$

and consequently, one finds maximum J_1 corresponding to $m/3$ resonance

$$J_1 \leq J_{max,m/3} = \left(\frac{4\sqrt{2}\rho^2}{9|b_2 b_3|\beta_x^2(s_2)\beta_x(s_1)^{3/2}L^2} \right)^{2/3} \quad (34)$$

The dynamic aperture of the machine is therefore

$$A_{dyn,m/3} = \sqrt{2J_{max,m/3}\beta_x(s)}$$

$$= \left(\frac{16\rho^2\beta_x(s)^{3/2}}{9|b_2 b_3|\beta_x^2(s_2)\beta_x(s_1)^{3/2}L^2} \right)^{1/3} \quad (35)$$

Eq. 35 gives the dynamic aperture of a sextuple and octupole strength determined case which is believed to be true for the most small emittance electron storage rings. Obviously, the dynamic aperture scales with the one third power of the sextupole and the octupole strength, respectively. If in a storage ring the perturbation from the sextupoles can be omitted, in a similar way one finds the maximum J_1 corresponding to $m/4$ resonance mode

$$J_1 \leq J_{max,m/4} = \frac{2\rho}{\sqrt{3}\beta_x(s_2)^2 L|b_3|} \quad (36)$$

and the corresponding dynamic aperture

$$A_{dyn,m/4} = \sqrt{2J_{max,m/4}\beta_x(s)} = \left(\frac{4\rho\beta_x(s)}{\sqrt{3}\beta_x(s_2)^2 L|b_3|} \right)^{1/2} \quad (37)$$

From eq. 37 one reads that the dynamic aperture, $A_{dyn,m/4}$, is proportional to the square root of the octupole strength. Usually, one has $A_{dyn,m/3} < A_{dyn,m/4}$.

Now I would like to spend some inks on the scenario of those particles whose motions do not satisfy the condition given by eq. 32. Once a particle begins to execute stochastic motion the phase mixing occurs, and the mapping given by eqs. 30 and 31 can be regarded as a Markov process [5], and in consequence, the possibility distribution function $\mathcal{F}(s, I)$ satisfies the Fokker-Planck equation:

$$\frac{\partial \mathcal{F}}{\partial s} = -\frac{\partial(\mathcal{A}\mathcal{F})}{\partial I} + \frac{1}{2}\frac{\partial^2(\mathcal{D}\mathcal{F})}{\partial I^2} \quad (38)$$

where $\mathcal{A} = << \Delta I >> /L$, $\mathcal{D} = << (\Delta I)^2 >> /L$, and the notation $<<>>$ denotes the average over phase θ. From eq. 30 one knows $\Delta I = K_0 sin\theta$, and obviously, one has $\mathcal{A} = 0$ and $\mathcal{D} = K_0^2/(2L)$. Due to the diffusion, needless to say, the amplitude of the particle's motion is increasing with the distance and finally the particle is lost on the vacuum chamber wall.

2.2 *Electron storage ring*

In an electron storage ring the physical picture is more complicated due to the synchrotron radiation damping. To treat this problem let's resort to the so-called *standard dissipative mapping* [2] which is different but similar to the standard mapping shown in eqs. 30 and 31, and expressed as follows:

$$\overline{I} = \exp(-\Gamma)I + K_0\mu\sin\theta \quad (39)$$

$$\overline{\theta} = \theta + \overline{I} \quad (40)$$

where $\Gamma = \frac{2L}{\tau_x c}$, τ_x is the damping time of the betatron oscillation in the horizontal direction, and $\mu = (1 - \exp(-\Gamma))/\Gamma$. Apparently, when $\Gamma \to 0$, eqs. 39 and 40 return to the standard mapping given by eqs. 30 and 31. The criterion for avoiding the onset of the stochastic motion in the dissipative system is given by

$$|\mu K_0| \leq 1 \quad (41)$$

The expressions for the dynamic apertures of the electron storage rings corresponding to the two expressions for the proton ones derived in the previous subsection are

$$A_{dyn,m/3} = \sqrt{2J_{max,m/3}\beta_x(s)}$$

$$= \left(\frac{16\rho^2\beta_x(s)^{3/2}}{9\mu|b_2 b_3|\beta_x^2(s_2)\beta_x(s_1)^{3/2}L^2} \right)^{1/3} \quad (42)$$

and

$$A_{dyn,m/4} = \sqrt{2J_{max,m/4}\beta_x(s)} = \left(\frac{4\rho\beta_x(s)}{\sqrt{3}\beta_x(s_2)^2 L\mu|b_3|} \right)^{1/2} \quad (43)$$

Eq. 42 has been compared with the numerical dynamic aperture simulation results of ALLADIN [6] and KEK Photon Factory [7], and the satisfactory comparison results are shown in ref. 8.

3 CONCLUSION

Considering delta function sextupole and octupole perturbations, analytical expression for the dynamic aperture of a circular machine is obtained by using the Chirikov criterion. It is shown that when the dynamics aperture is sextupole and octupole strength determined which is true for the most cases the dynamic aperture inversely scales with the one third power of the sextupole and octupole strength, respectively. The author thanks J. Le Duff for discussions.

4 REFERENCES

[1] R. Ruth, AIP conference proceedings, No. 153, p. 150.

[2] R.Z. Sagdeev, D.A. Usikov, and G.M. Zaslavsky, "Nonlinear Physics, from the pendulum to turbulence and chaos", harwood academic publishers, 1988.

[3] B.V. Chirikov, Physics Reports, Vol. 52, No. 5 (1979), p. 263.

[4] J.M. Greene, J. Math. Phys. 20 (1979), p. 1183.

[5] R.L. Stratonovich, "Topics in the theory of random noise", Vol. 1, Gordon and Breach Science Publishers Inc., 1963.

[6] J. Bridges, et al., *Particle Accelerators*, Vol. 28 (1990), p. 1.

[7] Y. Kobayash, et al., Proceedings of PAC93 (1993), p. 215, see also: M. Katoh, *Particle Accelerators*, Vol. 28 (1990), p. 17.

[8] J. Gao, LAL/RT 98-03.

Proceedings of the 1999 Particle Accelerator Conference, New York, 1999

THE INTRINSIC UPPER LIMIT TO THE BEAM ENERGY OF AN ELECTRON-POSITRON CIRCULAR COLLIDER

J. Gao, LAL, B.P. 34, F-91898 Orsay cedex, France

Abstract

In this paper we predict that there exists an intrinsic upper limit to the beam energy of an e^+e^- circular collider due to the beam-beam effects. The maximum beam energy is given by $E_{0,max} = 85.17\sqrt{N_{IP}}$(GeV), where N_{IP} is the number of the interaction points in the ring. It is concluded that LEP is the only machine on this planet which has the potential to test the validity of this theoretical prediction by reducing its interaction points to one.

1 INTRODUCTION

Since the first report on the interactions of 200MeV+200MeV e^+e^- beams in the single storage ring device, named AdA, was appeared in 1964 [1], the energy of the interacting electron and positron beams has increased by a factor of 300 in about 30 years. Due to synchrotron radiation the cost of an e^+e^- circular collider is increasing with energy squared [2]. It is taken for granted that e^+e^- collisions at energies beyond LEP II [3] can only be realized by using a linear collider. The questions one may ask, however, are that disregarding the problem of cost whether there exists an intrinsic upper limit for the beam energy of an e^+e^- circular collider, and if it exists, which value it takes. In this paper we try to answer these questions.

2 THEORY

Let's consider a storage ring of single beam (without interaction points and the beam-beam effects of course). Apparently, in this case we could not see any physical reason which limits the possible beam energy. As far as an e^+e^- storage ring collider is concerned the situation is quite different, and obviously, the difference is due to the additional interaction points and the beam-beam effects. To answer our questions it is worthwhile to start with the discussion on the beam-beam effects and the maximum beam-beam tune shift. The luminosity of a circular collider can be expressed as

$$\mathcal{L} = \frac{I_{beam}\gamma\xi_y}{2er_e\beta_y^*}\left(1+\frac{\sigma_y^*}{\sigma_x^*}\right) \tag{1}$$

where r_e is the electron radius, β_y^* is the beta function value at the interaction point, γ is the normalized particle energy, σ_x^* and σ_y^* are the bunch transverse dimensions after the pinch effect, respectively, I_{beam} is the circulating current of one beam, and

$$\xi_y = \frac{N_e r_e \beta_y^*}{2\pi\gamma\sigma_y^*(\sigma_x^*+\sigma_y^*)} \tag{2}$$

is the vertical beam-beam tune shift. At each interaction point particles in a bunch will be deflected transversely by the counter-rotating bunch. According to the linear theory of beam-beam dynamics [4], one knows that for two equal charge Gaussian bunches after each collision, the average beam-beam kicks of each particle in the horizontal and the vertical planes are expressed as follows

$$\delta x' = -\frac{2N_e r_e x}{\gamma\sigma_{x,+}^*(\sigma_{x,+}^*+\sigma_{y,+}^*)} \tag{3}$$

$$\delta y' = -\frac{2N_e r_e y}{\gamma\sigma_{y,+}^*(\sigma_{x,+}^*+\sigma_{y,+}^*)} \tag{4}$$

where $\sigma_{x,+}^*$ and $\sigma_{y,+}^*$ are the bunch transverse dimensions just before the interaction point. In fact, these kicks are *random* and they will move the zero-current equilibrium transverse beam sizes to the new values which depend on the bunch current [5]. Assuming that there are N_{IP} interaction points in the machine, and taking into account of these additional independent random kicks, one gets the new equilibrium horizontal and vertical emittances expressed as [5]:

$$\epsilon_x = \epsilon_{x0}\left(1-\frac{(e^2N_e\mathcal{K}_{IP,BB,x})^2N_{IP}\tau_x}{4T_0E_0^2}\right)^{-1} \tag{5}$$

and

$$\epsilon_y = \epsilon_{y0}\left(1-\frac{(e^2N_e\mathcal{K}_{IP,BB,y})^2N_{IP}\tau_y}{4T_0E_0^2}\right)^{-1} \tag{6}$$

where T_0 is the revolution period, E_0 is the beam energy, τ_x, τ_y are the horizontal and vertical damping time, respectively, ϵ_{x0}, ϵ_{y0} are the horizontal and vertical natural emittance, respectively, and

$$\mathcal{K}_{IP,BB,x} = \frac{\beta_x^*}{2\pi\epsilon_0\sigma_{x,+}^*(\sigma_{x+}^*+\sigma_{y,+}^*)} \tag{7}$$

$$\mathcal{K}_{IP,BB,y} = \frac{\beta_y^*}{2\pi\epsilon_0\sigma_{y,+}^*(\sigma_{x,+}^*+\sigma_{y,+}^*)} \tag{8}$$

where ϵ_0 is the permittivity of vacuum. For an isomagnetic ring, one gets

$$\epsilon_x = \epsilon_{x0}\left(1-\frac{3\epsilon_0R(eN_e\mathcal{K}_{IP,BB,x})^2N_{IP}}{2m_0c^2\gamma^5J_x}\right)^{-1} \tag{9}$$

and

$$\epsilon_y = \epsilon_{y0}\left(1-\frac{3\epsilon_0R(eN_e\mathcal{K}_{IP,BB,y})^2N_{IP}}{2m_0c^2\gamma^5}\right)^{-1} \tag{10}$$

where R is the local bending radius. For a flat bunch ($\sigma^*_{y,+} << \sigma^*_{x,+}$, in the following we restrict ourselves to this case), from eq. 10 one knows that

$$\sigma^*_{x.+}\sigma^*_{y.+} > \left(\frac{3RN_{IP}(eN_e\beta^*_y)^2}{8\pi^2\epsilon_0 m_0 c^2\gamma^5}\right)^{1/2} \quad (11)$$

Defining

$$H = \frac{\sigma^*_{x.+}\sigma^*_{y.+}}{\sigma^*_x\sigma^*_y} \quad (12)$$

where H is a measure of the *pinch* effect, and keeping in mind the physics of beam-beam effect at the interaction point, one can write

$$H = \frac{H_0\sqrt{N_{IP}}}{\gamma} \quad (13)$$

where H_0 is a constant and its value will be determined later. H is an important quantity and we will go back to it later. Combining eqs. 2, 11 and 13 one gets finally [5] (isomagnetic case)

$$\xi_y \leq \xi_{y,max} = H_0\sqrt{\frac{\gamma r_e}{6\pi R}} \quad (14)$$

or, for general cases

$$\xi_y \leq \xi_{y,max} = \frac{H_0}{2\pi\gamma}\sqrt{\frac{T_0}{\tau_y}} \quad (15)$$

We have therefore found the analytical expression for $\xi_{y,max}$ and explained the well-known phenomenon in circular colliders that $\xi_y \leq \xi_{y,max}$. The experimentally reached maximum H_0 is found to be about $\frac{1}{6} \times 10^6$. The validity of eqs. 14 and 15 has been demonstrated in ref. 5. On the road to arrive at eqs. 14 and 15 one has defined, expressed and used the pinch effect factor, H (see eq. 13). Now we go back to it and bear in mind that this quantity is one of the base stones of the analytical expressions for the maximum beam-beam tune shift which agree well with the experimental results. The reason why we call H a measure of the *pinch* effect lies in the fact that one has always (for the existing operational e^+e^- circular colliders) $H > 1$. The beam-beam effects not only increase the beam transverse emittances, as shown in eqs. 9 and 10, hence the transverse beam sizes, but also contribute to the maintenance of the beam transverse stabilities. One can imagine that one interaction point acts as a locally fastened belt on the beam "waist". At this point it is natural for one to raise his hand and ask the following question: *what happens if* $H \leq 1$? It is clear that by definition when $H = 1$ the pinch effect disappears, and the colliding beams in the collider act as a single beam in a storage ring (but with larger transverse equilibrium emittances due to the random beam-beam excitations). As for the case when $H < 1$ the physical intuition suggests us that this situation be unstable

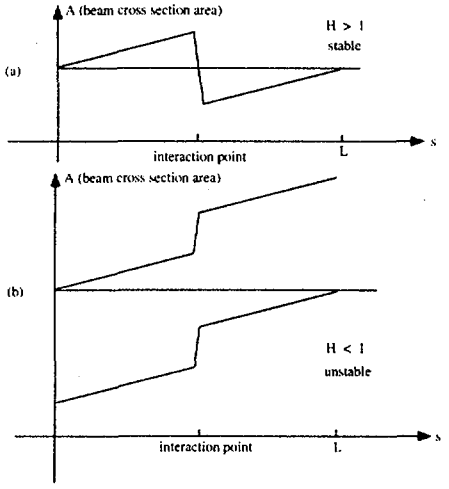

Figure 1: Schematical showing the difference between $H > 1$ and $H < 1$, where there is only one ineraction point in the ring for simplicity, and L is the perimeter of the ring.

since the interaction point explodes the beam as shown in Fig. 1. As bold as one can be we predict that

$$\gamma_{max} = H_0\sqrt{N_{IP}} \quad (16)$$

which corresponds to $H = 1$, as the intrinsic upper limit to the beam energy of an e^+e^- circular collider. For $N_{IP} = 1$ one gets from eq. 16 that $\gamma_{max} = H_0 = \frac{1}{6} \times 10^6$ or $E_0 = 85.17$GeV. Apparently, LEP has not met the limit due to its multi-interaction points ($E_{0,max}$(GeV)$= 85.17\sqrt{N_{IP}}$). It is interesting to predict that LEP II [6] (90GeV+90GeV) can not be realized if there is only one interaction point. In this planet LEP is the largest e^+e^- circular collider and the only machine having the potential to test this theoretical prediction by reducing the number of its interaction points to one.

From the point of view of the author the choice of an e^+e^- linear collider as the replacement to the circular one at energies beyond LEP II has its physical reason behind.

3 CONCLUSION

In this paper we predict an intrinsic upper limit to the beam energy in an e^+e^- circular collider due to beam-beam instabilities. The maximum energy is expressed as $E_{0,max} = 85.17\sqrt{N_{IP}}$(GeV). It is obvious that LEP is the only machine on this planet to have the potential to test this theoretical prediction by reducing the number of its interaction points to one.

4 REFERENCES

[1] C. Bernardini, "Bruno Touschek and AdA", in "ADONE a milestone in the particle way", edited by V. Valente, Frascati Physics Series Vol. VIII (1997), p. 1.

[2] B.H. Wiik, "e^+e^- at the TeV Scale", *ibid.*, p. 171.

[3] L. Foà, "Physics at LEP", *ibid.*, p. 151.

[4] E. Keil, "Beam-beam dynamics", CERN 95-06, p. 539.

[5] J. Gao, "Analytical expression for the maximum beam-beam tune shift in electron storage rings", *Nucl. Instr. and Methods* **A413** (1998), p. 431.

[6] S. Myers, "LEP status and plans", Proceedings of PAC95, Washington, USA (1995), p. 476.

COAXIAL DISC WINDOWS FOR A HIGH POWER SUPERCONDUCTING CAVITY INPUT COUPLER

S. Chel, M. Desmons, C. Travier, CEA/DSM/DAPNIA/SEA Saclay
T. Garvey, P. Lepercq, R. Panvier, CNRS/IN2P3/LAL Orsay

Abstract

A $\lambda/2$ coaxial L-band window has been tested up to 1 MW (1 ms pulses), both at room temperature and at 80 K. Dielectric losses were measured. A travelling wave window with lower dielectric losses has been fabricated.

1 INTRODUCTION

In the framework of the TESLA collaboration, Saclay and Orsay are designing an alternate input power coupler. The aim is to develop a simplified version of the present TTF coupler, in order to reduce the cost. The way to achieve this simplification is to consider a fixed (non tunable) and rigid (non flexible) coupler. As part of this effort, a coupler test stand including a 80 K cryostat was constructed [1], and several coupler parts were designed and tested. This paper presents the experimental results concerning a $\lambda/2$ disc window. It also describes the design of a travelling wave (TW) disc window.

2 $\lambda/2$ DISC COAXIAL WINDOW

The simplest coaxial window one can imagine is a ceramic disc brazed inside the 50 Ω coaxial pipe. In order to be self-matched, the ceramic should be half a wavelength thick. Using WESGO Al300 alumina which has a permittivity $\epsilon_r = 9$ at the designed frequency of 1.3 GHz (as given by the vendor), the window was designed with the parameters given on table 1. The inner conductor is made of copper, while the outer conductor is made of kovar, an alloy which has a linear thermal expansion coefficient very close to that of the ceramic and is therefore often used in ceramic/metal assemblies. The kovar piece is then TIG welded to the stainless steel copper coated outer conductor as shown in fig. 1. The ceramic is coated with a thin layer of TiN. This window was fabricated by SICN [2].

The main advantages of this type of window are its relative simplicity, its robustness, the absence of electric field perpendicular to the ceramic surface which is favorable for avoiding multipactor, and the ease with which the window can be cleaned prior to its assembly on the cavity. The potential drawbacks are the high electric field at the braze location and the high dielectric losses due to the large volume of ceramic used.

3 WINDOW TEST CONDITIONS

The window was mounted on the test stand presented in reference [1]. It is inserted on the test line between a door-knob type and an antenna type waveguide to coax transition as shown schematically on fig. 2. The diagnostics used are 2 electrons pick-ups located on both sides of the window and 2 photomultipliers located as shown on fig. 2.

Table 1: Windows characteristics

Characteristics		
	$\lambda/2$	TW
Inner diameter (mm)	26.8	75.6
Outer diameter (mm)	61.6	142.2
Ceramic thickness (mm)	38.4	10
Performances		
Bandwidth (MHz) (S11 < 0.1)	80	80
Ratio between max field at brazing and max field in coax	1	0.2
Avg. dielectric losses (W) at 1 MW (TESLA pulse)	44	6.5

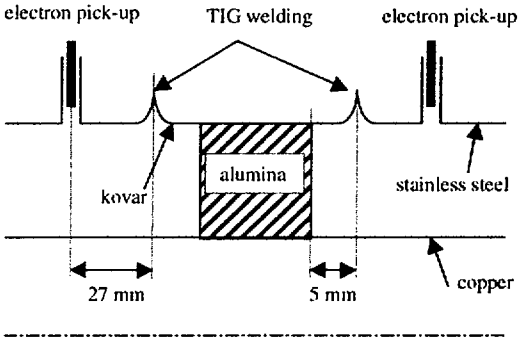

Figure 1: $\lambda/2$ disc coaxial window

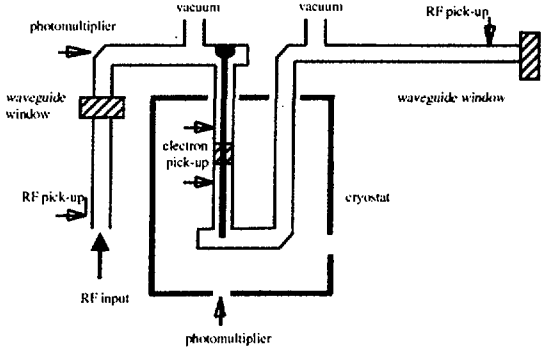

Figure 2: Coupler test stand

The present capability of the power source allows tests at a peak power of 1 MW, for pulses of 800 μs and a repetition rate of 0.1 Hz. The system runs continuously and all signals (RF power, vacuum, electrons, light, temperatures) are recorded for each pulse. This $\lambda/2$ window was tested for almost 5 months between August 1998 and January 1999, this period corresponding to 990,983 pulses. For each pulse, 80 parameters are recorded, so that the total amount of data represents 1.3 Gbytes. Since the analysis of such a huge amount of data cannot be made with standard spreadsheet softwares, PAW [3] is used.

The window was tested under all possible conditions: at room temperature and at liquid nitrogen temperature, with standing and travelling wave rf input, with vacuum on both side and with atmospheric pressure on one side. The result of all these tests are presented in the next sections.

4 TEST UNDER STANDING WAVE CONDITIONS

By using a short-circuit at the end of the line, one can operate the test stand under standing wave conditions thus simulating what is happening during the filling of the cavity. The initial conditioning of the window was done under these standing wave conditions. It took nearly 30,000 pulses to reach the 1 MW level. At that point, while the system was processing at 1 MW, an incident occurred that exhibited large electron, light and vacuum signals, downstream of the window. Unfortunately, the software interlock that would normally reduce the input power in such case didn't work. As this event happened at the beginning of the week-end, the system ran for the whole week-end at 1 MW. Due to large electron emission at or near the downstream side of the window, the power was fully reflected at this location. After that unfortunate event, it took more than 300,000 pulses to recondition the window up to 1 MW. Once conditioned, we cannot observe any systematic and significant electron or light signal at any power level. At a very erratic rate, one can see some electron signal when the electric field is maximum at the window surface, especially on the side that was potentially damaged by the event described above. To illustrate this behaviour, fig. 3 shows that, while running at 1 MW, some strong electron signal can be seen. After a few tens of pulses these signals are processed away. The figure shows that these multipacting events are seen on the vacuum recording, on the light signal and on the temperature indicator located on the outer conductor in the vicinity of the window. However, all these signals do not allow one to know precisely if the emission is occurring exactly at the window surface (braze location) or somewhat further in the conductor and especially at the kovar/stainless steel weld that is only 5 mm downstream. The behaviour of the window under standing wave conditions is exactly the same both at room temperature and at 80 K.

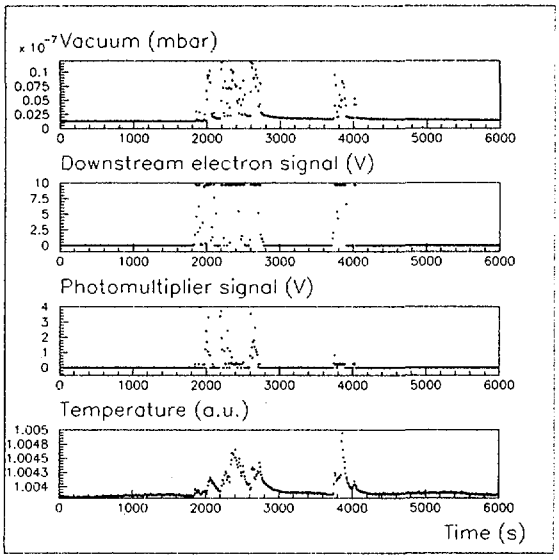

Figure 3: An example of multipactor behaviour at 1 MW (standing wave conditions)

5 TEST UNDER TRAVELLING WAVE CONDITIONS

Under travelling wave operation, one can observe electron activity on both sides of the window. However as shown on fig. 4, the signal is much stronger and the power range is wider on the damaged side. Fig. 4 also shows that this multipactor can be processed: after 180,000 pulses, signal was strongly diminished on the downstream damaged side and completely disappeared on the upstream side. We didn't wait long enough to see, if it would also disappear on the downstream side. Here again, the behaviour is similar at room temperature and at 80 K.

6 DIELECTRIC LOSSES IN THE WINDOW

Since the window is thermally connected to the liquid nitrogen cooled shield, the total heat load it produces is of major concern. In the case of the $\lambda/2$ window, the main part of the heat load is due to the dielectric losses. By choosing properly the distance between the superconducting cavity and the window itself, the dissipation at LN2 temperature can be reduced. For the complete TESLA pulse (filling time of 530 μs and beam time of 800 μs), the dissipated power Pdiss in the dielectric is evaluated to be: 8.79 * tanδ * Average incident power with a distance = (2N+1)λ/4 and 5.83 * tanδ * Average incident power with a distance = Nλ/2. In the standing wave case and for a distance corresponding to (2N+1)λ/4, we measured a dissipation corresponding to 1.1% of the average input power, from which we infer that tanδ = 5.8 10^{-4}.

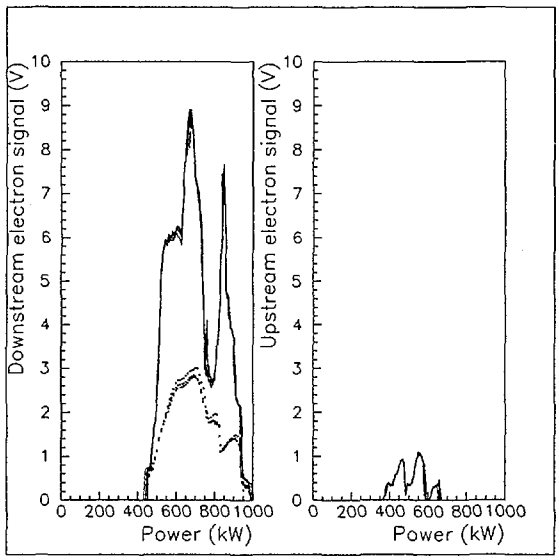

Figure 4: Multipactor as a function of power for TW operation, upstream and downstream sides: at some time (line) and 180,000 pulses later (dots).

7 TRAVELLING WAVE WINDOW

In order to reduce the dielectric losses in the ceramic, one can use a thinner ceramic and/or reduce the electric field inside the ceramic. With a thin ceramic, the matching is achieved by adding some inductive or capacitive components on the coax on both side of the ceramic. The simplest solution is to use some bumps on the coaxial inner conductor as proposed in reference [4]. Here, we are trying to find a design where the ceramic would be completely shielded from the electrons coming from the cavity to avoid the potential problems seen, for example, at CEBAF [5]. The advantages of the window, shown on fig. 5, are a low field inside ceramic and therefore low losses, a low field at the brazing location, no field components perpendicular to the ceramic surface, no direct exposure of the ceramic to cavity electrons, while the main drawback are its relative complexity, its large diameter, and the difficulty to clean it. Two windows that are now ready to be tested, were fabricated by SICN [2]: one where titanium is used for the outer conductor brazed on the ceramic and the other for which copper is used. In both cases, the inner conductor is made of plain copper.

8 CONCLUSION

In this paper we present the results of the high power tests made on the coaxial $\lambda/2$ window that we designed and fabricated. The first results are encouraging. Though a failure of the control system at the beginning of the conditioning led to a metallic coating of one side of the window (the precise nature of this coating is under investigation), it was later on capable of sustaining 1 MW of peak power, both

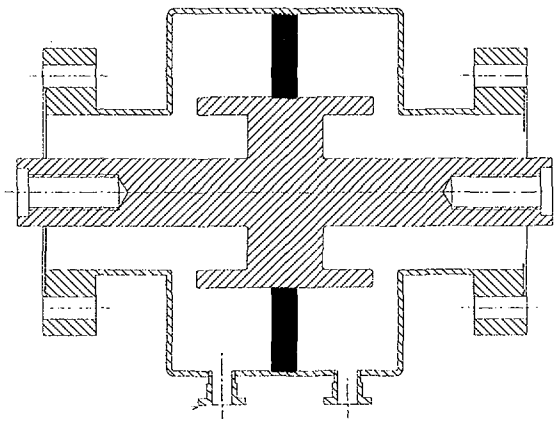

Figure 5: Travelling wave window

under travelling and standing wave operation, both at room temperature and at 80 K , and both under vacuum and atmospheric pressure. Up to 400 kW, the window works without any signs of electron activity. Between 500 kW and 1 MW, the travelling wave operation reveals some electron activity that we cannot attribute with certainty to the window. It will be necessary to test a second, identical, window that was fabricated to confirm these results. It will then be necessary to fabricate a new window with a slightly different design (replace kovar by titanium or copper, and replace the TIG welding by electron beam welding) to see whether it is possible to eliminate electron activity over the full power range.

The dielectric losses were measured and proved to be too high for operation at the TESLA repetition rate and peak power needed for the superstructures [6]. To improve this situation, it would be necessary to use ceramics with a higher purity. These ceramics exist but the brazing to metal is more difficult. Another solution is to use the travelling wave window that was presented in this paper, and which will soon be tested.

9 ACKNOWLEDGEMENTS

We would like to thank all the people at IN2P3 and DAPNIA involved in this work for the design, construction and operation of the test stand, especially F. Blot, D. Braud, P. Dufresne, A. Hamdi, M. Kalmykow.

10 REFERENCES

[1] S. Chel et al., EPAC98, p. 1882.

[2] SICN, BP 1, 38113, Veurey-Voroize, France.

[3] PAW, CERN Program Library Long Writeup Q121, 1995.

[4] X. Hanus, A. Mosnier, Proc. of the 7^{th} Workshop on RF superconductivity, Gif sur Yvette, October 17-20, 1995, p. 701.

[5] T. Powers, P. Kneisel, ibid, p.. 713.

[6] M. Ferrario, J. Sekutowicz, EPAC98, p. 1876.

Proceedings of the 1999 Particle Accelerator Conference, New York, 1999

RF PULSED TESTS ON 3GHZ NIOBIUM CAVITIES

J. Le Duff, C. Thomas*, G. Bienvenu, H.Sun† LAL, Orsay, France
M. Fouaidy, IPN, Orsay, France , R. Parodi, INFN, Genova, Italy

Abstract

The achievable limiting RF field for S-Band and L-Band superconducting cavities is still an open question today. Previous studies on Sn and In have shown that a surface magnetic field B_s higher than the thermodynamical critical field B_c might be reached. The ultimate limiting field is then the superheating field B_{sh} (B_{sh} = 240 mT or E_{acc} = 60 MV/m for Nb at T= 0 K). However, the maximum accelerating field observed so far is in the range E_{acc} = 37-40 MV/m for the best 1.3 GHz Nb cavities. A dedicated facility (NEPAL Supra Test Facilty) is currenly used at LAL for measuring B_{sh} on bulk Nb 3 GHz cavities supplied by INFN-Genova. High power pulses (4.5 μs, up to 5 MW) are used to reach B_{sh} before cavity thermal breakdown occurs. A method for analyzing the response of a SRF cavity when subjected to pulsed high RF power was developed and the corresponding numerical simulation results were validated by comparison to experimental data. This technique is successfully applied to detect E_{acc} and B_{sh} at which the cavity magnetic breakdown occurs. Magnetic penetration depth (λ) measurements were also performed with a low RF level test bed and the corresponding data analyzed then compared to theoretical predictions.

1 INTRODUCTION

The maximum achieved accelerating fields in SRF cavities are usually limited by field emission and thermal breakdown. These two limits have been pushed back thanks to improvements of niobium purity, cavity preparation, assembling and conditionning techniques. In principle, a theoretical limit of the surface field higher than B_c (i.e B_c = 200 mT or 50MV/m accelerating field E_{acc} for TESLA shape bulk niobium (Nb) cavities at T = 0 K) is expected in CW mode of operation. Previous RF measurements performed on indium and tin samples and the corresponding theoretical estimation have shown that $B_s \geq B_c$ might be reached [1]. Moreover, the fundamental limit B_{sh} of bulk Nb is now close to being reached [2]. Due to lack of sufficient experimental data on B_{sh} for Nb, it is important to measure this parameter precisely.

2 SUPERHEATING FIELD AND PENETRATION DEPTH

In this section, we briefly summarize the useful relationships dealing with the predictions of B_{sh} and λ according to different theories.

* Email: cthomas@lal.in2p3.fr
† visitor, IHEP, Beijing, PRC

2.1 Superheating Field

For Type-II superconductors such as niobium, subjected to an external magnetic field B_a (static or slowly varying), the Meissner effect persists up to the first critical field, B_{c1}. For B_a lying between B_{c1} and B_{c2}, normal conducting areas are nucleated : this thermodynamic state is called the mixed state. Beyond B_{c2}, superconductivity is completely destroyed. Moreover, in the case of non-zero B_a, the transition from superconducting to normal conducting state is of first order. In this case, superheating is possible and a magnetic field (B_{sh}) higher than the critical field B_{c1} could then be sustained by the superconducting material. The superheating field B_{sh} is related to the critical thermodynamic field B_c. According to Ginzburg-Landau (GL) theory [3], we distinguish two kinds of superconductors depending on the value of the material's GL parameter $\kappa_{GL} = \frac{\lambda_{GL}}{\xi_{GL}}$ where ξ_{GL} is the GL coherence length:

For type I superconductors, $B_{sh} \approx \frac{0.89}{\sqrt{\kappa_{GL}}} B_c$.

For type II, $B_{sh} \approx 0.75 B_c$.

Note that niobium, which is a type II superconductor but with a peculiar behaviour due to a κ value close to the critical value $\kappa_{GL}^{Nb} \simeq \kappa_{GL}^{c} = \frac{1}{\sqrt{2}}$, we have :

$$B_{sh} = 1.2 * B_c \tag{1}$$

2.2 Penetration depth

The London magnetic penetration depth $\lambda_L(0)$ at absolute zero is given, according to the well-known phenomenological London theory, by $\lambda_L(0) = \sqrt{\frac{m}{\mu_0 n_s e^2}}$ where m, e are respectively the mass and charge of the electron and n_s is the density per unit volume of super electrons at T = 0 K. The temperature dependence of the cooper pair density, introduced in the two fluid model by Gorter-Casimir (GC), results in an empirical temperature-dependent London penetration depth : $\lambda_{GC}(t) = \lambda_{L0} \frac{1}{\sqrt{1-t^4}}$, where t is the reduced temperature ($t = T/T_c$) with reference to the material critical temperature T_c. This expression was derived in the London limit where $\xi_0 \gg \lambda$ and is not valid in the neighbourhood of T_c (i.e t close to 1) [4]. Ginzburg and Landau [3] showed that the penetration depth depends on the material purity, or equivalently the electron mean free path, leading to the following asymptotic expressions :

- for "clean" superconductors ($l \gg \xi_0$)

$$\lambda_{GL}(t) = \frac{\lambda_L(0)}{\sqrt{2(1-t)}} \tag{2}$$

- for "dirty" superconductors ($l \ll \xi_0$)

$$\lambda_{GL}(t) = \frac{\lambda_L(0)}{\sqrt{2}} \sqrt{\frac{\xi_0}{1.33 l}} \frac{1}{\sqrt{(1-t)}} \tag{3}$$

where ξ_0 is the BCS coherence length and l the mean free path of a normal electron. Note that measuring the magnetic penetration depth allow us to determine l and to obtain the RRR of our cavity in-situ. Direct RRR measurements on cavities [5] will be used to cross-check the first results. Moreover, we plan to measure both B_{sh} and λ (Eq. 3) before and after cavity heat treatment with Ti gettering (i.e material purification), hence we will be able to check the validity of the relationship given by Eq. 1 (i.e. B_{sh} doesn't depend on κ_{GL}).

3 METHOD OF B_{SH} MEASUREMENT

In most case, the maximum accelerating field is limited, in DC or long RF pulsed mode ($1 - 10$ms) by cavity thermal breakdown. To circumvent this problem, we use RF pulses of duration $\tau_p = 1 - 4.5\mu$s which are much shorter than the characteristic time needed for cavity thermal breakdown or quench induced by anomalous RF losses to occur ($\simeq 100\mu$s [6]). In order to achieve a good transfer efficiency between the RF source and the cavity, a strong external coupling is needed (i.e $Q_{ext} = 5.10^4$). As long as the cavity is in the superconducting state ($Q_0(4.2K) \simeq 7.10^7$), the cavity decay time $\tau = \frac{Q_L}{\omega}$, where Q_L is the loaded quality factor, is dominated by the external coupling (i.e $\tau \simeq \frac{Q_{ext}}{\omega}$). When a thermal or magnetic breakdown occurs, Q_0 jumps instantaneously to $10^6 - 10^5$ and consequently τ decreases. The transmitted power integral $U_t = \int A \exp -\frac{t}{\tau} dt$, which is proportional to the incident power integral U_i, when the cavity is in the superconducting state, shows a deviation from the linear behaviour when the cavity quenches (i.e transition to the normal state) as illustrated in Fig. 1. The point, where such a deviation (eq. jump of U_t) is initiated and referred to as "B" in this figure, corresponds exactly to the quench field. Note that other methods of quench field measurements are not appropriate to our test stand [7].

4 EXPERIMENTAL APPARATUS AND PRELIMINARY RESULTS

In order to reach a high accelerating field, we use a 3 GHz-35 MW klystron with a maximum pulse length of 4.5μs. The experimental set-up block diagram is shown in Fig. 2. Data acquisition of all the experimental parameters and processing (RF signal integration) is performed using a dedicated Labview^{TM} program.

Experimental runs were performed and the corresponding preliminary results are displayed in Fig. 3. The shape of the experimental curve is close to the expected simulation results (see Fig. 1). More precisely , we clearly observe a linear part of U_t versus U_i up to a critical value of U_i ($U_i^c \simeq 1.4 - 1.5$ J). Moreover as expected, at this value U_t decreases sharply (cavity magnetic breakdown) when U_i is slightly increased, reaching a plateau at $U_t \simeq 0.6\mu$J for $U_i \geq 1.5$ J. Note that a precise value of the maximum E_{acc} and hence B_s at which the cavity magnetic breakdown occurs could not be deduced from these results at the time being because of some calibration uncertainties.

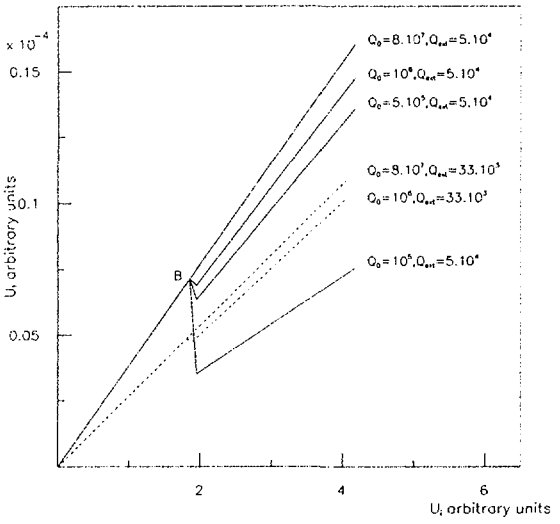

Figure 1: Simulation of the variation of the transmitted power integral versus the incident power integral.

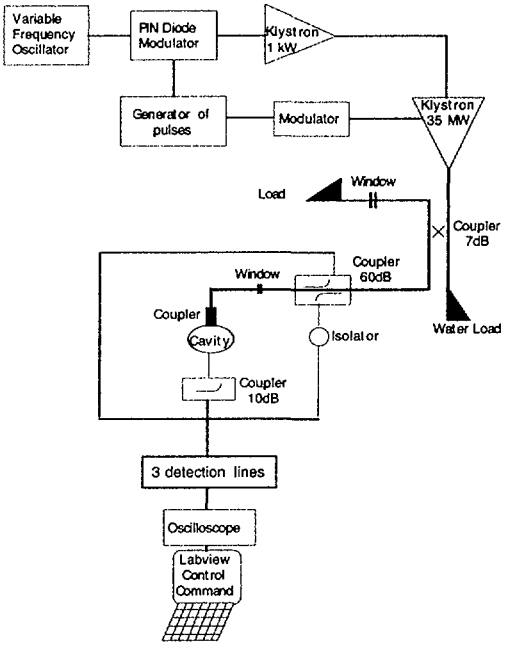

Figure 2: Schematic of experimental set-up

5 MAGNETIC PENETRATION DEPTH : METHOD AND RESULTS

The cavity resonant frequency is influenced by the magnetic penetration depth which is a temperature dependent parameter. More precisely, the reactive component of the cavity surface impedance X is related to the resonant fre-

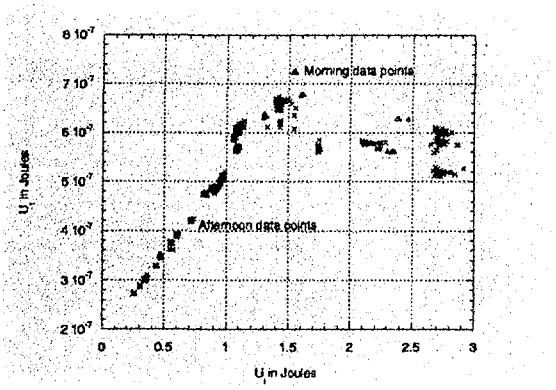

Figure 3: Integral of transmitted power versus integral of incident power (performed at T = 4.2 K on cavity CAT2)

quency f by the formula : $X = 2G\frac{(f-f_0)}{f_0}$ where G is the geometric factor and f_0 is the frequency of an ideal cavity (perfectly conducting). Moreover, X is proportional to the frequency and magnetic penetration depth ($X = 2\pi f \mu_0 \lambda$). Consequently, starting at an initial temperature $T_0 = 4.2K$ and recording the cavity frequency shift due to temperature variation, we can easily deduce the corresponding $\Delta\lambda$:

$$\Delta\lambda(T) = \lambda(T) - \lambda(T_0) = \frac{G}{\pi\mu_0}\frac{\Delta f}{f(T_0)^2} \qquad (4)$$

This procedure was used and the corresponding data (160 data points) analysed and compared (Fig. 4) to the theoretical relationships of GL (Eq. 3) or GC. These results clearly show that GL theory fits the data better than the GC theory : the corresponding mean standard deviation are respectively 23.1nm and 22.2nm for GC and GL theories. Note that the two fitting parameters are very sensitive to the Nb critical temperature T_c (T_c was ajusted by trial and error in the range : 9.1 K-9.4 K), and the optimum value was 9.3 K. This figure is close to published data (T_c = 9.3 K) [8]. The measured $\lambda_{GL}(4.2K)$ = 33nm is in good agreement with previous results [9] leading to a mean free path l = 670 Å and hence a Residual Resistivity Ratio RRR = 10. The estimated RRR obtained from Nb impurities contents (O, C, N) [10] is 40. The apparent discrepency between the RRR deduced from λ_{GL} and the estimated one could be explained by RRR decrease near the Nb surface [11]. Finally, the corresponding experimental GL parameter is $\kappa_{GL}^{exp} = 1.1$ which is close to κ_{GL}^{c}.

6 ACKNOWLEDGEMENTS

We would like to thank J.N.Cayla for his technical support, G.Arnaud, Ph.Dufresne and M.Roch for their assistance concerning vacuum and cryogenics as well as the IPN Superconducting cavity group and S.Buhler for their helpful advice. A special thank to B.Mouton for his friendly help.

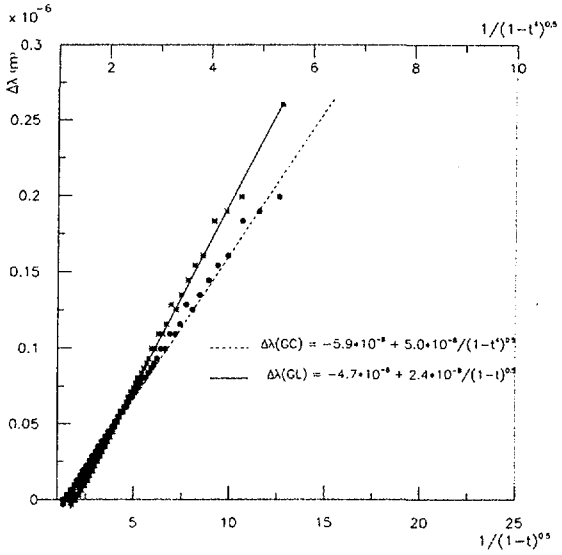

Figure 4: Effect of temperature on the relative magnetic penetration depth for $T_c = 9.3K$ [8] for cavity GEN1 ($\chi^2_{GL} = 1.58$ and $\chi^2_{GC} = 21.08$ respectively)

7 REFERENCES

[1] T.Yogi, G.J.Dick, J.E.Mercereau, Phys. Rev. Letters 39, (1977), pp826-829

[2] E.Kako et al. "Improvement of cavity performance by electropolishing in the 1.3GHz Nb superconducting cavities", this conference

[3] V.L.Ginzburg and L.D.Landau, JETP 20 (1950), p1064.

[4] J.Bardeen, L.N.Cooper, J.R.Schrieffer, Phys.Rev. 108 (1957), pp1175-1204.

[5] H.Safa et al., "RRR Mapping of SRF cavities by a magnetometric method", Proc. of 8^{th} SRF Workshop, Abano Terme, (1997).

[6] T. Junquera et al., "Thermal stability analysis of superconducting RF cavities", Advances in Cryogenic Eng., Vol 43.

[7] T.Hays, H.Padamsee, "Measuring the RF critical fields of Pb, Nb, Nb_3Sn", SRF 980804-06, LNS, Cornell Univ..

[8] M Cyrot and Davor Pavuna, "Introduction to superconductivity and High-Tc Materials", (1992), p113.

[9] B.Bonin, "Materials for superconducting cavities", CERN96-03, p194.

[10] M.Fouaidy, Private communication.

[11] C.Antoine et al., "Nuclear Microprobe studies of impurities segregation in Niobium used for radiofrequency cavities", Proc. of 8^{th} SRF Workshop, Abano Terme, (1997).